NETWORK NEUROSCIENCE

an open access journal

Citation: Nelson, M. C., Royer, J., Lu, W. D., Leppert, I. R., Campbell, J. S. W., Schiavi, S., Jin, H., Tavakol, S., Vos de Wael, R., Rodriguez-Cruces, R., Pike, G. B., Bernhardt, B. C., Daducci, A., Misic, B., & Tardif, C. L. (2023). The human brain connectome weighted by the myelin content and total intra-axonal cross-sectional area of white matter tracts. *Network Neuroscience*, *7*(4), 1363–1388. https://doi.org/10.1162/netn_a_00330

DOI: https://doi.org/10.1162/netn_a_00330

Supporting Information: https://doi.org/10.1162/netn_a_00330; https://portal.conp.ca/dataset?id=projects/mica-mics; https://github.com/TardifLab/Weighted-SC-Networks

Received: 3 March 2023
Accepted: 19 July 2023

Competing Interests: The authors have declared that no competing interests exist.

Corresponding Author:
Mark C. Nelson
mark.nelson3@mail.mcgill.ca

Handling Editor:
Alex Fornito

The MIT Press

RESEARCH

The human brain connectome weighted by the myelin content and total intra-axonal cross-sectional area of white matter tracts

Mark C. Nelson[1,2], Jessica Royer[1,2], Wen Da Lu[2,3], Ilana R. Leppert[2], Jennifer S. W. Campbell[2], Simona Schiavi[4], Hyerang Jin[1,2], Shahin Tavakol[1,2], Reinder Vos de Wael[1,2], Raul Rodriguez-Cruces[1,2], G. Bruce Pike[5], Boris C. Bernhardt[1,2], Alessandro Daducci[4], Bratislav Misic[1,2], and Christine L. Tardif[1,2,3]

[1]Department of Neurology and Neurosurgery, McGill University, Montreal, QC, Canada
[2]McConnell Brain Imaging Centre, Montreal Neurological Institute and Hospital, Montreal, QC, Canada
[3]Department of Biomedical Engineering, McGill University, Montreal, QC, Canada
[4]Department of Computer Science, University of Verona, Verona, Italy
[5]Hotchkiss Brain Institute and Departments of Radiology and Clinical Neuroscience, University of Calgary, Calgary, Canada

Keywords: Connectomics, Network neuroscience, Structural connectivity, Functional connectivity, White matter, Myelin, Microstructure-weighted imaging

ABSTRACT

A central goal in neuroscience is the development of a comprehensive mapping between structural and functional brain features, which facilitates mechanistic interpretation of brain function. However, the interpretability of structure-function brain models remains limited by a lack of biological detail. Here, we characterize human structural brain networks weighted by multiple white matter microstructural features including total intra-axonal cross-sectional area and myelin content. We report edge-weight-dependent spatial distributions, variance, small-worldness, rich club, hubs, as well as relationships with function, edge length, and myelin. Contrasting networks weighted by the total intra-axonal cross-sectional area and myelin content of white matter tracts, we find opposite relationships with functional connectivity, an edge-length-independent inverse relationship with each other, and the lack of a canonical rich club in myelin-weighted networks. When controlling for edge length, networks weighted by either fractional anisotropy, radial diffusivity, or neurite density show no relationship with whole-brain functional connectivity. We conclude that the co-utilization of structural networks weighted by total intra-axonal cross-sectional area and myelin content could improve our understanding of the mechanisms mediating the structure-function brain relationship.

AUTHOR SUMMARY

For computational network models to provide mechanistic links between brain structure and function, they must be informed by networks in which edge weights quantify structural features relevant to brain function. Here, we characterized several weighted structural networks capturing multiscale features of white matter connectivity including total intra-axonal cross-sectional area and myelin density. We describe these networks in terms of edge weight distribution, variance, and network topology, as well as their relationships with each other, edge length, and function. Overall, these findings support the joint use of structural networks weighted by the total intra-axonal cross-sectional area and myelin content of white

matter tracts in structure-function models. This thorough characterization serves as a benchmark for future investigations of weighted structural brain networks.

INTRODUCTION

The quest to relate human structural and functional brain networks spans the spectrum of spatial scale and repertoire of data modalities absolutely. At the macroscale, the human brain can be modeled as an anatomical network of discrete neuronal populations (nodes) interconnected by white matter fibers (edges) (Sporns, 2011). Coordinated spatiotemporal patterns of neuronal activity unfolding upon this structural backbone are fine-tuned by white matter microstructure (Hodgkin & Huxley, 1952; Huxley & Stämpfli, 1949; Moore et al., 2020; Pumphrey & Young, 1938) and form the basis of cognition and behavior (Biswal et al., 1995; Greicius et al., 2003; Hampson et al., 2006; Liégeois et al., 2019; S. M. Smith et al., 2009; van den Heuvel et al., 2009). Increasingly, MRI facilitates in vivo measurement of multiscale properties of both brain structure (e.g., Alexander et al., 2019; Drakesmith et al., 2019; Jeurissen et al., 2019; Mancini et al., 2020) and function (e.g., Finn et al., 2019; Friston, 2011; Gordon et al., 2017; Liu et al., 2022). Diffusion MRI streamline tractography and resting-state functional MRI are often respectively used to estimate structural and functional connectivity (SC and FC) networks. Network science provides a framework to bring these fundamentally different substrates into a common space where their features can be quantified (Fornito et al., 2016; Sporns, 2010; Suárez et al., 2020) and used to probe the mechanisms mediating human brain function (e.g., Cabral et al., 2017; Fornito et al., 2015).

Streamline:
The contiguous set of 3D points produced by a tractography algorithm and representing the reconstructed trajectory of a white matter pathway.

Tractography:
A method or algorithm that applies some model to diffusion MRI data to reconstruct a 3D visual representation of the white matter pathways of the brain.

SC network edges can be weighted by a range of MRI-derived metrics quantifying white matter microstructural features relevant to brain function, including voxel-level estimates of tissue diffusivity (e.g., Caeyenberghs et al., 2016), neurite density (H. Zhang et al., 2012), axon diameter distributions (Alexander et al., 2010; Assaf et al., 2008), myelin content (Heath et al., 2018; Mancini et al., 2020), and the g-ratio (ratio of inner/outer diameters of myelinated axons) (Stikov et al., 2011, 2015), as well as tract/bundle-level measures of axonal cross-sectional area (Daducci, Dal Palù, et al., 2015; R. E. Smith et al., 2015). Subsets of these metrics have been investigated using a microstructure-weighted connectomics approach (Boshkovski et al., 2021; Caeyenberghs et al., 2016; Deligianni et al., 2016; Frigo et al., 2020; Mancini et al., 2018; Messaritaki et al., 2021; Schiavi et al., 2020; van den Heuvel et al., 2010; van den Heuvel & Sporns, 2011; F. C. Yeh et al., 2016). We aim to extend this work by providing a comprehensive assessment of the fundamental characteristics of a range of standard and state-of-the-art weighted structural brain networks, including a network weighted by myelin.

Tractometry:
A method for mapping the voxel-level values of a volumetric brain map onto the streamlines of a tractogram.

Tractogram:
The 3D image representing the collection of streamlines reconstructed by a tractography algorithm.

Edge weight:
The value assigned to the inter-nodal connections of a network that describes an explicit feature of each connection such as physical length or connection strength.

The networks considered here can be grouped into two classes: those computed with tractometry (Bells et al., 2011) and those computed directly from the streamline weights in a tractogram, that is, streamline-specific. We consider three examples of the latter: (a) the number of streamlines (NoS); and two methods that optimize the streamline weights in a tractogram to increase specificity for white matter structural features; (b) spherical-deconvolution informed filtering of tractograms (SIFT2) (R. E. Smith et al., 2015); and (c) convex optimization modeling for microstructure informed tractography (COMMIT) (Daducci et al., 2013; Daducci, Dal Palù, et al., 2015). SIFT2 and COMMIT were designed to overcome known limitations of streamline counts (Girard et al., 2014; Jones, 2010; Jones et al., 2013). While the edge weights in all three networks generally capture white matter features relevant to connection strength, SIFT2 and COMMIT more specifically quantify the total intra-axonal cross-sectional area of white matter

tracts (henceforth referred to as *edge caliber*). To date, COMMIT and SIFT2 have not been compared to NoS with uniform connection density (Frigo et al., 2020; Schiavi et al., 2020; C. H. Yeh et al., 2016). Thus, it remains unclear how the edge weights themselves affect network topology.

In contrast, tractometry allows network edge weights to be derived from any volumetric brain image that is coregistered to the tractogram. This increase in methodological flexibility comes at the expense of anatomical specificity. Tractometry is unable to resolve the separate contributions of individual fiber populations to the aggregate value of a voxel. Given that an estimated 90% of white matter voxels at typical diffusion MRI resolutions (~2 mm) contain multiple fiber populations (Jeurissen et al., 2012), the quantitative link between white matter microstructure and essentially all tractometry-derived edge weights is biased by partial volume effects.

Partial volume effect:
A "smoothing" or "blurring" imaging artifact whereby the data corresponding to sub-voxel-level features are lost or averaged as a result of the limited resolution of an imaging system.

In this work, tractometry is combined with a diffusion tensor model (Basser, 1995; Basser et al., 1994) to derive networks weighted by FA (fractional anisotropy) and RD (radial diffusivity), which respectively quantify the degree of diffusion anisotropy (i.e., directional dependence) and diffusion magnitude perpendicular to the major axis. The crossing fiber problem described above is also known to limit the ability of diffusion tensor models to quantify white matter features (De Santis et al., 2014; Tournier et al., 2011). Additional tractometry networks examined here include a network weighted by ICVF (intracellular volume fraction) computed with NODDI (neurite orientation dispersion and density imaging) (H. Zhang et al., 2012), as well as a network weighted by the longitudinal relaxation rate R_1 ($1/T_1$) derived from a quantitative T_1 map. The edge weights in this network are myelin-weighted, as R_1 has been shown to correlate with histology-derived myelin content (Mancini et al., 2020; Mottershead et al., 2003).

This characterization of weighted structural brain networks is carried out as follows: (a) within-network features of edge weight distribution and variance; (b) edgewise relationships with FC, edge length, and myelin (R_1); and (c) topological features of small-worldness, rich club, and network hubs. Importantly, uniform binary connectivity is enforced across all weighted network variants, that is, the underlying binary connectivity map is identical. This allows the edge weights themselves to drive the characterization.

Small-worldness:
A topological network feature characterized by a low number of edges or connections separating distal nodes (short path length) alongside high connectivity between neighboring nodes (high local clustering).

Rich club:
The tendency for highly connected (high degree) nodes to be more densely connected among themselves than nodes of a lower degree.

RESULTS

In 50 healthy adults (27 men; 29.54 ± 5.62 years; 47 right-handed), structural brain networks were estimated from multi-shell diffusion MRI data with probabilistic tractography. Each subject's structural network was used to compute eight SC networks (Table 1) in which edges were weighted by NoS, SIFT2, COMMIT, FA, RD, ICVF, R_1, and LoS (edge length computed as the mean length of streamlines). NoS, SIFT2, COMMIT, and LoS correspond to streamline-specific metrics, whereas networks weighted by FA, RD, ICVF, and R_1 were computed using tractometry. The edge weights in NoS, SIFT2, and COMMIT networks were normalized by node volume. Additionally, a static FC network was derived for each subject by zero-lag Pearson cross-correlation of nodewise resting-state time series. Unless otherwise stated, all results shown correspond to networks parcellated with the Schaefer-400 cortical atlas (Schaefer et al., 2018) and include 14 subcortical nodes.

Structural Brain Networks Vary in the Distribution of Their Edge Weights

Group-level networks weighted by NoS, SIFT2, and COMMIT show spatially distributed patterns of high-magnitude edge weights and noticeably accentuate within-module connectivity

Table 1. Summary of structural network weights

Short name	Long name	Method	Data source	Interpretation
LoS	Length of streamlines	Streamline-specific	Diffusion MRI	Mean length of the streamlines connecting two nodes
NoS	Number of streamlines	Streamline-specific	Diffusion MRI	Number of streamlines connecting two nodes; connection strength
SIFT2	Spherical-deconvolution informed filtering of tractograms	Streamline-specific	Diffusion MRI	Fiber density from spherical deconvolution summed across streamlines; connection strength
COMMIT	Convex optimization modeling for microstructure informed tractography	Streamline-specific	Diffusion MRI	Total intra-axonal cross-sectional area summed across streamlines; connection strength
R_1	Longitudinal relaxation rate	Tractometry	Multimodal MRI (diffusion + relaxometry)	$R_1 = 1/T_1$; index of tissue myelin content
FA	Fractional anisotropy	Tractometry	Diffusion MRI	Diffusion directional dependence
RD	Radial diffusivity	Tractometry	Diffusion MRI	Diffusion perpendicular to the principal axis
ICVF	Intracellular volume fraction	Tractometry	Diffusion MRI	Neurite density

(Figure 1). Modules correspond to the seven-canonical resting-state networks (Yeo et al., 2011) plus the subcortex. These patterns are hallmarks of FC networks and are observed in the FC network shown here. The contrast between high- and low-magnitude edge weights is most evident in COMMIT. By comparison, the spatial variation of edge weight distribution in the tractometry networks is smoother with more pronounced regional concentrations. R_1 is highest in the edges connecting the visual module to itself and to the rest of the brain; and lowest within the subcortex and between the subcortical and limbic modules. The surface plot shows the highest concentration of R_1 in the white matter projections of posterior cortical regions.

Group-level edge weight distributions are summarized with respect to two important organizational patterns of brain function (Figure 2A): within and between resting-state modules (Yeo et al., 2011); and along the principal functional gradient (Margulies et al., 2016). NoS, SIFT2, and COMMIT mirror FC in both plots with greater edge weight magnitude within module, especially within unimodal modules. R_1, ICVF, FA, and RD generally mirror LoS with the reverse trend: higher between module and lowest in unimodal modules. This suggests that tractometry-derived networks may be influenced by edge length to a greater extent.

Subject-level edge weight distributions in R_1, ICVF, FA, and RD are near normal and network-specific (Figure 2B). They differ in both the magnitude (R_1 > ICVF > FA > RD) and the dynamic range (FA and ICVF > R_1 and RD) of their edge weights. In contrast, NoS, SIFT2, and COMMIT distributions are highly skewed and tend to be much lower in magnitude (dashed line). This effect is greatest in COMMIT, suggesting that the optimization performed by COMMIT exerts a stronger scaling effect than SIFT2. These results support the conclusion that the structural networks considered here quantify subsets of white matter features that are at least partially nonoverlapping.

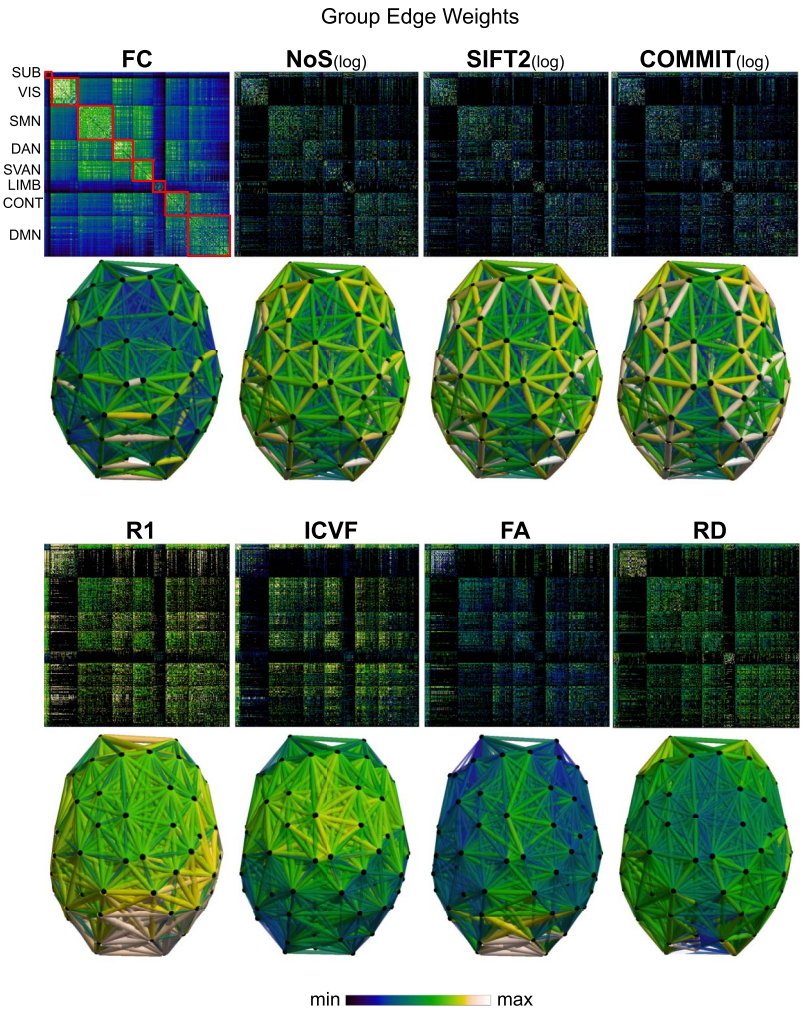

Figure 1. Edge weight spatial distribution. Connectivity matrices of group-level edge weights for FC (functional connectivity), NoS (number of streamlines), SIFT2 (spherical-deconvolution informed filtering of tractograms), COMMIT (convex optimization modeling for microstructure informed tractography), R_1 (longitudinal relaxation rate), ICVF (intracellular volume fraction), FA (fractional anisotropy), RD (radial diffusivity), and LoS (mean length of streamlines). Each network is composed of 414 nodes as defined by the Schaefer-400 cortical parcellation and 14 subcortical ROIs. Nodes are grouped into the canonical resting-state modules (Yeo et al., 2011) plus the subcortex: SUB (subcortex), VIS (visual), SMN (somatomotor), DAN (dorsal attention), SVAN (salience ventral attention), LIMB (limbic), CONT (control), and DMN (default mode). 3D cortical surfaces (shown below) of group-level edge weights in the Schaefer-100 parcellation generated with BrainNet Viewer (Xia et al., 2013). Edge diameter and color indicate weight magnitude. The edge weights in NoS, SIFT2, and COMMIT networks were $\log_{10}$ transformed for visualization.

Edge Weights in Streamline-Specific Networks Are More Variable

Edge weight variance was quantified using the quartile coefficient of dispersion (CQD) because of its robustness to outliers and skewed data. The CQD is computed from the first and third quartiles as the following: $CQD = (Q_3 - Q_1)/(Q_3 + Q_1)$.

Intra-subject variance is roughly twofold greater in NoS, SIFT2, and COMMIT relative to LoS and FC; and an order of magnitude greater than R_1, ICVF, FA, and RD in all subjects (Figure 3A). COMMIT is the highest overall. Subjects are more tightly clustered in all weighted

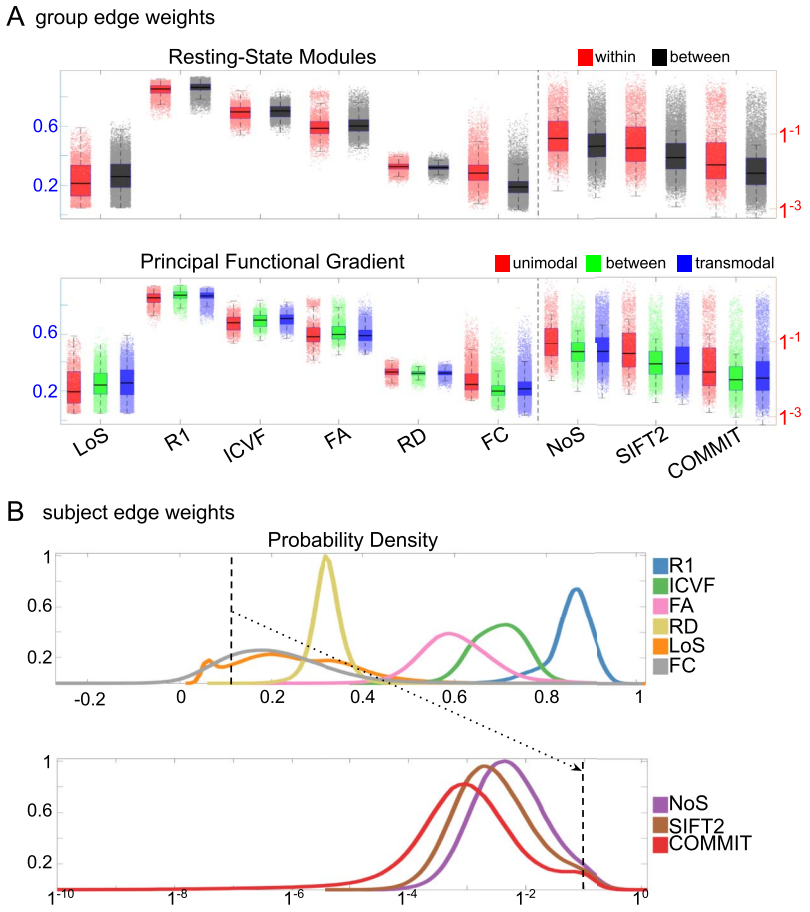

Figure 2. Edge weight distribution. (A) Distribution of group-level edge weights binned by (top) within- and between-module; (bottom) unimodal, transmodal, and between. Unimodal is defined as the VIS and SMN modules. Transmodal is defined as the DMN, CONT, DAN, and SVAN modules. (B) Probability density of pooled subject-level edge weight distributions. R_1, ICVF, FA, RD, LoS, and FC are shown on a linear x-axis (top), and NoS, SIFT2, and COMMIT are shown on a logarithmic x-axis (bottom). All networks were normalized to the range [0, 1] by dividing by the subject-level max for visualization.

SC networks, relative to FC: intra-subject CQD values span roughly a fourfold greater range in FC. This suggests that individual diversity of functional connectivity is not necessarily reflected in the variability of their structural networks. These patterns are repeated for *inter-subject* variance. However, FC shows a small subset of highly variable edges with roughly fourfold greater CQD than the maximum values observed in COMMIT; that is, the most subject-specific connections are functional. The very low edge weight variability in R1, ICVF, FA, and RD is in part due to the widespread blurring effect (partial voluming) resulting from the tractometry computation.

In general, inter-subject edge weight variance is more spatially distributed in SC networks relative to FC (Figure 3B). COMMIT shows the highest mean CQD over the entire cortex and subcortex. NoS, SIFT2, and COMMIT all show lateral-medial and posterior-anterior cortical gradients. Mean CQD in FC shows the highest concentration in medial inferior frontal cortex and, to a lesser extent, the expected pattern of high variance in association cortex. The most variable subcortical regions include the hippocampus, amygdala, and accumbens.

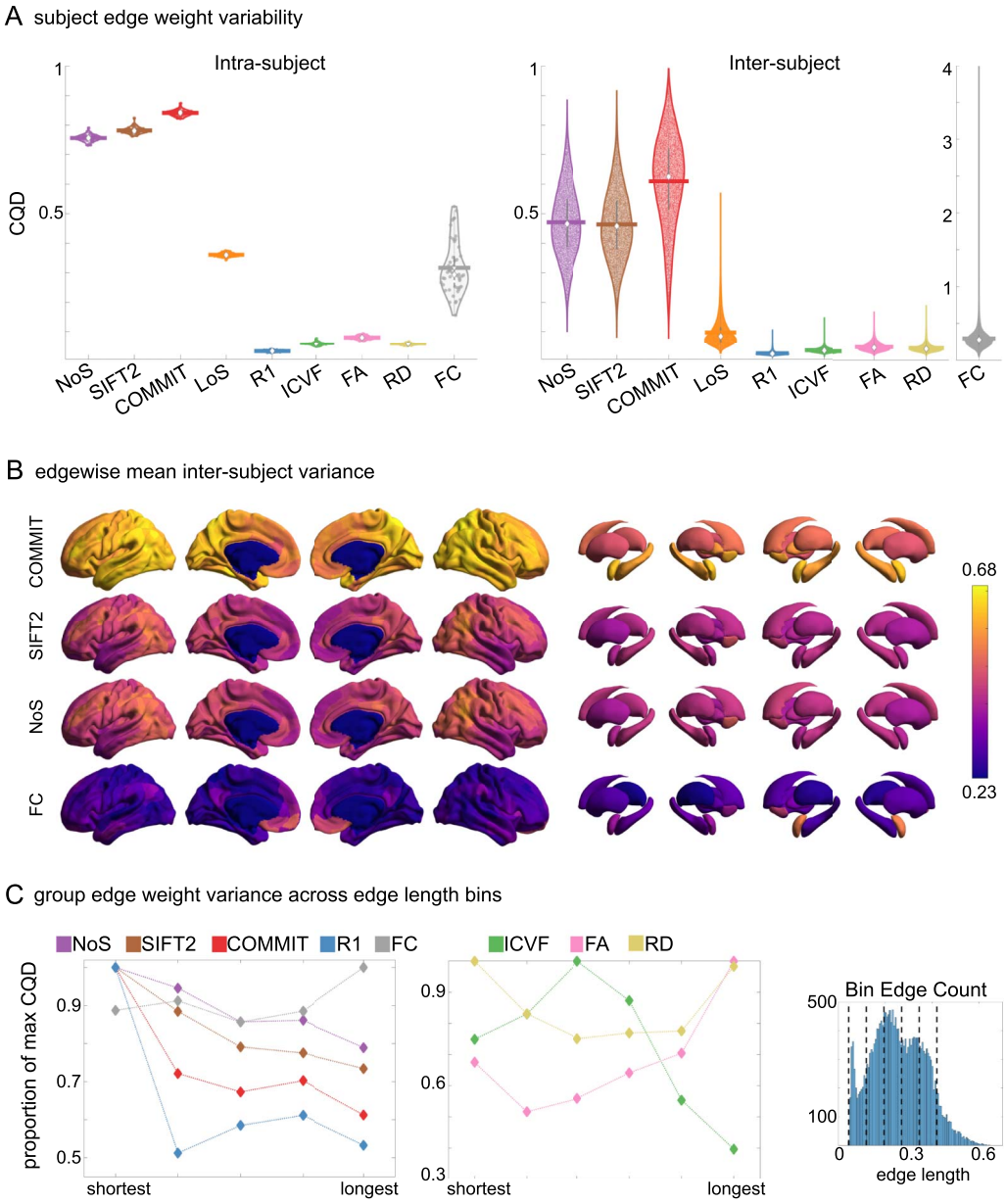

Figure 3. Edge weight variability. Variability is quantified using the coefficient of quartile dispersion (CQD). (A) Violin distributions of intra-subject (left) and inter-subject (right) edge weight variance. Colored data points respectively correspond to individual subjects ($N = 50$) and edges ($N = 8{,}549$). (B) Surface projections of edgewise mean inter-subject variance for cortical nodes in the Schaefer-400 parcellation (left) and 14 subcortical nodes (right). Cortical and subcortical surfaces were respectively generated with BrainSpace (Vos de Wael et al., 2020) and ENIGMA toolboxes (Larivière et al., 2021). (C) The proportion of within-network max CQD is shown across edge length bins for FC, NoS, SIFT2, COMMIT, and R_1 (left), as well as ICVF, FA, and RD (middle). Edge weights are grouped into six bins according to edge length, as illustrated by the histogram (right). The edges of bins 1–5 were linearly spaced of width, w. The edges of the final bin were of width 3w.

Many features of brain networks (e.g., connection probability, weight magnitude) are known to vary with edge length. Here, we examined the relationship between edge weight variability and edge length by computing the CQD within subsets of group-level edge weights binned according to their edge length (Figure 3C). Edge weight variance in NoS, SIFT2, COMMIT, and R_1 is highest in the shortest edges and decreases with edge length. ICVF roughly follows the same pattern. FA and RD instead show the highest variability in the longest edges.

Overall, the edge weights in streamline-specific SC networks (NoS, SIFT2, and COMMIT) show greater contrast both within and across subjects. SC networks show network-dependent relationships between edge weight variance and edge length. Shorter edges are more variable in myelin- and connection-strength-weighted networks, and longer edges are more variable in networks with edge weights derived from a diffusion tensor model.

To complement the above results, a supplemental analysis was performed using intraclass correlation to quantify edge weight variance within each edge weight (Supporting Information Figure S9).

Opposing Correlations with Function in Connection-Strength- and Myelin-Weighted Networks

Shifting to inter-network edge weight relationships shows that SC networks are differentially related to FC (Figure 4A). Importantly, we also see that all brain networks (SC and FC) are strongly and differentially related to edge length at the subject and group levels. Correlations with edge length are negative for NoS, SIFT2, COMMIT, RD, and FC; and positive for R_1, ICVF, and FA. Correlation magnitude is strongest in group-level COMMIT ($\rho \approx -0.8$). To account for this strong obscuring effect, we recomputed correlations using residual edge weights following linear regression of edge length (Figure 4B). NoS, SIFT2, and COMMIT remain positively associated (group-level $\rho \approx 0.35$) and R_1 remains negatively associated with FC (group-level $\rho \approx -0.22$). Correlation magnitude was reduced following linear regression of edge length in all

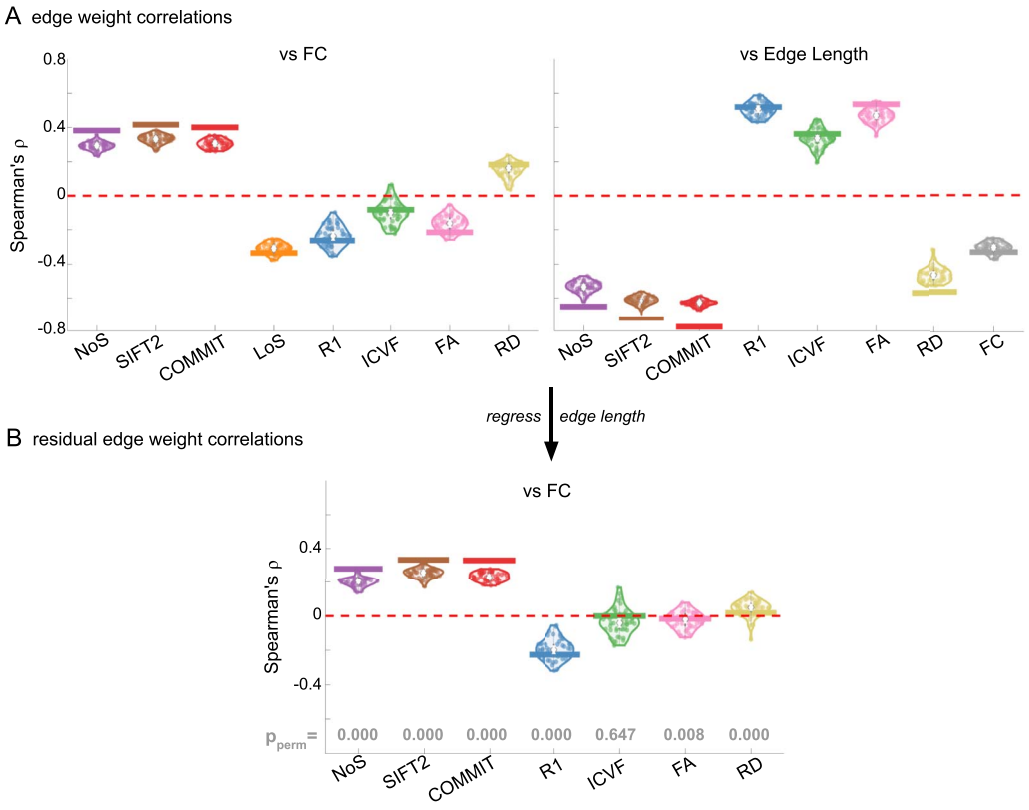

Figure 4. Edge weight correlations with FC and edge length. (A) Violin distributions of edgewise Spearman's rank correlations of all networks with FC (left) and edge length (right). (B) Violin distributions of edgewise Spearman's rank correlations of residual edge weights in all networks with residual edge weights in FC. Residual edge weights were computed by linear regression of edge length. Colored data points and bars respectively indicate subject-level and group-level correlations. P_{perm} gives the one-sided p value obtained from permutation testing (Supporting Information Figure S7).

cases. ICVF, FA, and RD are reduced to 0, suggesting that they may not be useful in modeling whole-brain FC. These results support the idea that R_1-weighted SC networks provide complementary information to NoS, SIFT2, and COMMIT about the brain structure-function relationship.

Edge Caliber and Myelin Content Are Inversely Related

Here, we ask how R_1, which we refer to as the myelin-weighted network, is related to the connection-strength-weighted network COMMIT. Edge-length regressed residual edge weights in NoS, SIFT2, and COMMIT show a negative association with R_1 residuals for all subjects and at the group level, which is strongest in COMMIT (group-level $\rho \approx -0.29$) (Figure 5A). This suggests an edge-length-independent inverse relationship between white matter structural features related to connection strength and myelin content.

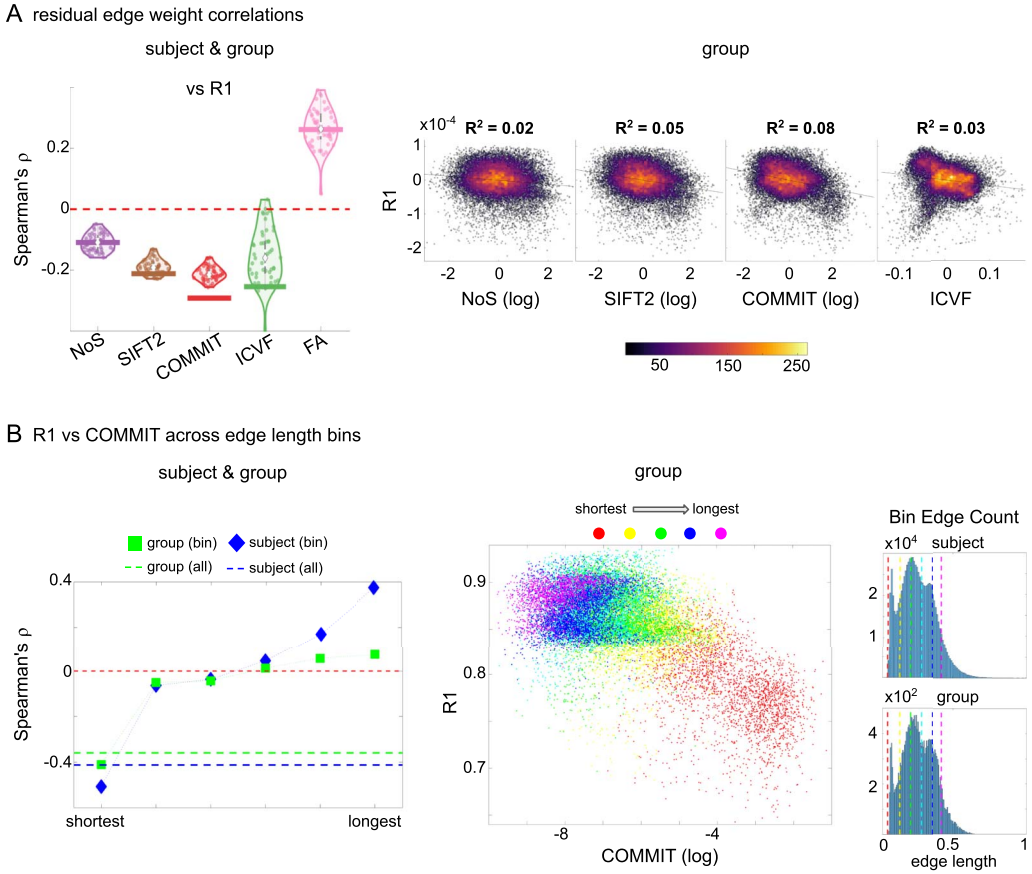

Figure 5. The myelin-dependence of structural brain networks. (A) Violin distributions (left) of edgewise Spearman's rank correlations with the myelin-weighted network R_1. Residual edge weights are compared following linear regression of edge length. Colored data points and bars respectively indicate subject-level and group-level correlations. Heat scatterplots (right) of group-level residual edge weights in R_1 as a function of NoS (left), SIFT2 (left middle), COMMIT (right middle), and ICVF (right). The best fit linear curve is shown in black, and R^2 (coefficient of determination) is reported. Data color indicates density. Permutation testing provided a one-sided p value of $P_{perm} = 0.000$ for all edgewise correlations (Supporting Information Figure S8). (B) Line plot (left) of edgewise Spearman's rank correlation of edge weights in R_1 versus COMMIT across edge length bins. Group-level and subject-level are respectively shown in green and blue. The square and diamond markers connected by dotted lines show binned correlation values, and the horizontal dashed green and blue lines mark the correlation values for all edges pooled together. Scatterplot (middle) of group-level edge weights in R_1 as a function of COMMIT with data points colored by bin identity. Histograms (right) illustrating subject- and group-level edge length bins.

Computing correlations of edge weights (not residuals) within edge length bins allows the inverse relationship between R_1 and COMMIT to be traced to the shortest edges of the network (group $\rho \approx -0.40$, subject $\rho \approx -0.50$). As edge length increases, this relationship is reduced to 0, then becomes strongly positive in the longest subject-level edges ($\rho \approx 0.39$). The scatterplot of group-level R_1 versus COMMIT (middle) shows decreasing COMMIT and increasing R_1 with increasing edge length. All together, these results support an inverse relationship between the edge caliber and myelin content of a given white matter tract. This can be partly explained by the differential dependence of these structural features on edge length: longer tracts tend to be more myelinated with lower total intra-axonal cross-sectional area. However, this relationship is robust to controlling for edge length supporting an intrinsic dependence between these white matter features.

In addition, we show that our R_1-weighted network corresponds well with a previously reported (Boshkovski et al., 2021) R_1-weighted structural connectome (Supporting Information Figure S13).

Divergent Small-Worldness, Hubness, and Rich Club in Weighted Structural Networks

Graph theory:
The study of graphs, which are mathematical structures used to model pairwise relationships between objects.

Characteristic path length:
The average shortest path length between all pairs of nodes in the network.

In this final section, we apply network analysis tools (Rubinov & Sporns, 2010) based on graph theory (Fornito et al., 2013; Sporns, 2018) to group-level weighted SC networks. This facilitates high-level interpretation of general features of network communication such as integrative versus segregative processing and the economy of network organization. Although the high material and metabolic cost of brain tissue naturally tends to favor local connectivity (high clustering), short overall network path length is achieved through a small number of relatively expensive long-range connections (Bullmore & Sporns, 2012). These edges and the nodes they interlink form a densely connected network core known as the rich club (van den Heuvel & Sporns, 2011). While the general proclivity for high local clustering gives rise to segregated functional modules, the rich-club nodes act as network communication hubs supporting inter-modular integration (Collin et al., 2014; de Reus & van den Heuvel, 2014; Griffa & van den Heuvel, 2018; Kim & Min, 2020; van den Heuvel & Sporns, 2013). Thus, small-world network topology (high clustering and low path length) (Bassett & Bullmore, 2006, 2017) supports both integrative and segregative processing at a minimum of wiring cost, and the underlying scaffold of hub brain regions tends to show high centrality, low path length (high closeness), and low clustering (van den Heuvel et al., 2010).

Here, we report normalized small-worldness, normalized rich-club curves, and nodal hubness (Figure 6). Normalized small-worldness (S) is computed as the quotient of normalized measures of clustering coefficient (C/C_{null}) and path length (L/L_{null}).

Clustering coefficient:
The fraction of triangles around an individual node, that is, the fraction of a node's neighbors that are also neighbors with each other.

All group-level weighted SC networks show the normalized small-world property ($S > 1$) of higher clustering and lower path length than would be expected by chance (Figure 6A). Small-worldness is highest in COMMIT ($S \approx 2.5$) and lowest in R_1, ICVF, FA, and RD ($S \approx 1.6$). In contrast, all weighted SC networks did not show a canonical rich club (Figure 6B). Relative to the tractometry and binary SC networks, the normalized rich-club coefficient (ϕ_{norm}) was much higher in magnitude in NoS, SIFT2, and COMMIT. A rich club was detected in these networks across a large range of degree (k) levels ($150 < k < 300$). ϕ_{norm} was maximal at $k \approx 265$ in COMMIT. A rich club was also detected across a similar range of k levels in ICVF and across k in the range [250, 300] for RD, albeit with much lower magnitude ϕ_{norm}. However, no clear rich club was observed in R_1 or FA. In fact, the rich-club curves for these networks are roughly symmetric about the $\phi_{norm} = 1$ line relative to COMMIT. A densely connected core was of course recovered in all weighted SC networks (uniform binary connectivity), but these

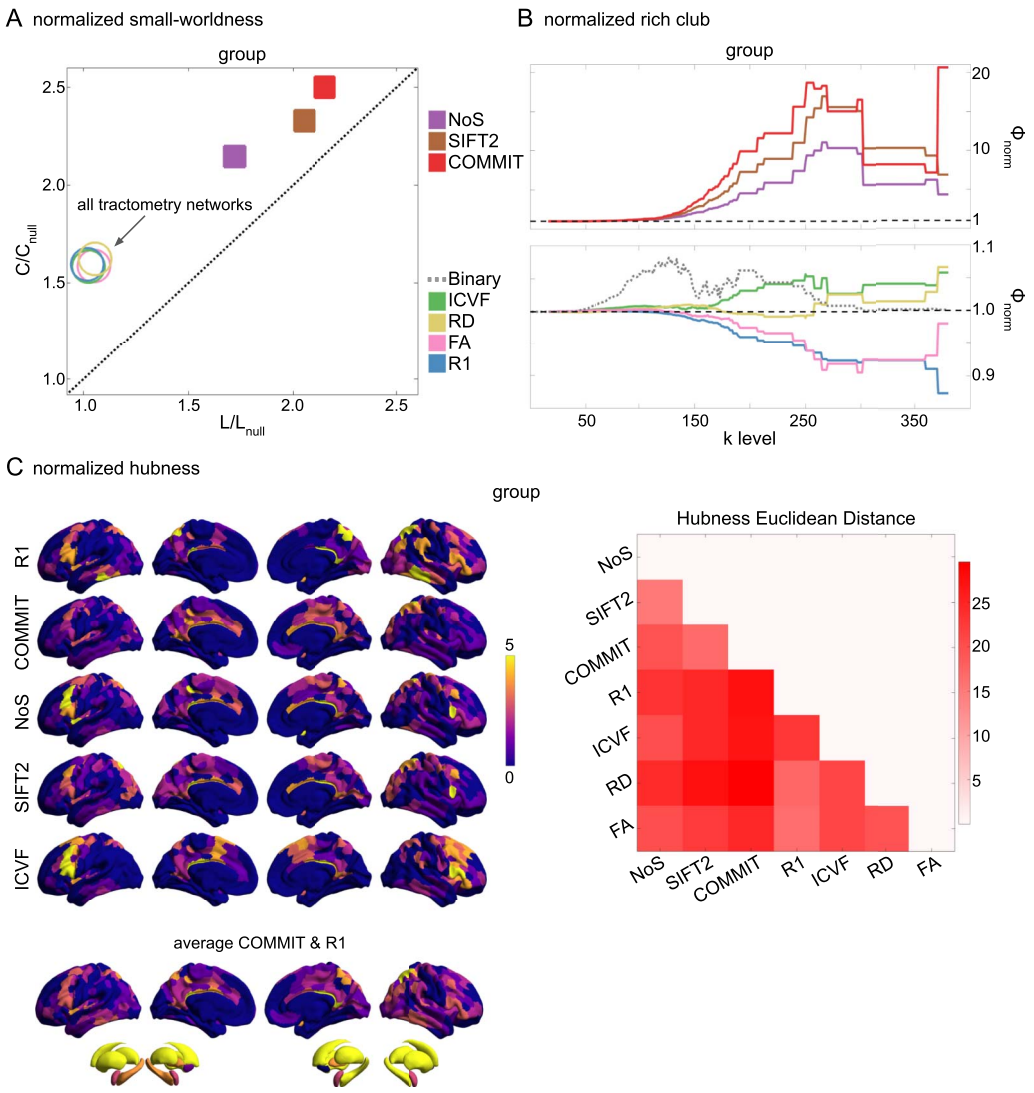

Figure 6. Group-level network topology. (A) Small-worldness was estimated in all structural networks: clustering coefficient was normalized within each node, averaged across nodes (C/C_{null}), then plotted as a function of normalized characteristic path length (L/L_{null}). Topology measures averaged across 50 degree- and strength-preserving null networks were used for normalization. Networks above the identity line (dotted black) are characterized by the small-world attribute. Tractometry networks are indicated by the arrow. (B) Normalized rich-club curves are shown for COMMIT, NoS, and SIFT2 (top), as well as ICVF, RD, FA, and R_1 (bottom). A single binary network (dotted gray line) is also shown (bottom) as binary connectivity was uniform across weighted networks. The normalized rich-club coefficient (ϕ_{norm}) was computed across the range of degree (k) and normalized against 1,000 null networks (degree-preserving for binary and degree- and strength-preserving for weighted networks). A ϕ_{norm} value > 1 (horizontal dashed black lines) over a range of k indicates the presence of a rich club. (C) Nodewise hubness scores are projected onto Schaefer-400 cortical and 14-ROI subcortical surfaces. Scores (0–5) were computed for each node as +1 point for all nodes in top 20% strength, betweenness, closeness, and eigenvector centrality, as well as bottom 20% clustering coefficient. The matrix (right) shows the Euclidean distance between all pairs of nodal hubness vectors.

results suggest that its interconnecting edges were consistently weaker than would be expected by chance in R_1 and FA. By comparison, a rich club was observed in the binary SC network across the very large range of k [50, 300]. This supports two important concepts: (1) SC network edge weights can provide an additional layer of information useful for refining the topology of binary SC. (2) Different methods for computing SC network edge weights yield diverse network topology.

Weighted SC networks show network-dependent spatial topology of hubness scores (Figure 6C). The COMMIT and R1 averaged surface shows prominent hubs distributed throughout the brain including the frontoparietal network. Nearly all of the subcortex showed a hubness score of 4 or greater in all networks. The Euclidean distance between hubness score vectors (right) was lower for COMMIT and SIFT2 than for either network with NoS. Of the streamline-specific networks, NoS was more similar to both R1 and IVCF. Overall, these results illustrate the considerable impact that edge weighting can have on network topology.

DISCUSSION

Structure-function brain models provide a flexible framework for investigating the mechanistic relationship between human brain structure and function in vivo, yet the interpretability of these models is currently limited by a lack of biological detail. Here, we assemble a thorough characterization of structural brain networks weighted by a range of quantitative MRI metrics capturing the macro- and microscopic features of white matter tracts. Notable trends included the following: (a) greater edge weight contrast and skewed (heavy-tailed) distributions in the streamline-specific networks NoS, SIFT2, and COMMIT; (b) whole-brain correlations with FC in networks weighted by connection strength (positive) and myelin (negative) that were robust to controlling for edge length; (c) whole-brain inverse relationships with myelin for networks weighted by connection strength and neurite density independent of edge length; and (d) the absence of a rich club in R_1 and FA networks. All weighted SC networks showed a strong spatial dependence and small-world architecture. Collectively, these results support the overall conclusion that SC networks weighted by edge caliber (e.g., SIFT2 and COMMIT) and myelin (e.g., R_1) can be used to quantify nonoverlapping subsets of white matter structural features related to FC, supporting their joint utilization in modeling function.

Interpretable Measures of Connection Strength Provided by COMMIT and SIFT2

A principal goal of this work is to identify what, if any, advantage over NoS is provided by the global optimization methods SIFT2 and COMMIT. NoS has previously been used to inform the strength of interregional coupling in computational models of function (e.g., Honey et al., 2009). However, important limitations restrict model interpretation. Besides suffering from a range of biases related to the position, size, shape, and length of white matter tracts (Girard et al., 2014), NoS varies as a function of tracking parameters, limiting its specificity for white matter structural features (Jones, 2010; Jones et al., 2013).

SIFT2 and COMMIT reportedly restore the quantitative link between connectome edge weights and white matter structural features related to connection strength. COMMIT and SIFT2 solve for the effective cross-sectional area (i.e., signal fraction) of each streamline using different approaches. COMMIT uses the global diffusion signal to optimize these values, whereas SIFT2 seeks to fit the streamline density throughout the white matter to the fiber densities estimated using spherical deconvolution. Thus, while both methods rely on the simplifying assumption that streamline features are invariant along their length, SIFT2 additionally requires that the estimates of fiber density derived from the fiber orientation distribution (FOD) are biologically accurate.

These networks also differ in the computation of their edge weights: SIFT2 is computed as the simple sum of streamline weights, whereas COMMIT is computed as the length-weighted sum of streamline weights. Indeed, our analysis methods do not permit us to make strong claims as to the relationship between these methodological differences and our observed

results; however, we do show that both SIFT2 and COMMIT display comparable but not identical fundamental characteristics to NoS. This supports the use of SIFT2 or COMMIT in place of NoS as a measure of connection strength, which brings with it improved biological interpretability.

Myelin Complements Connection Strength in Predicting FC

Despite the differences between COMMIT, SIFT2, and NoS, our results indicate that their edge weights show roughly equivalent positive correlations with FC over the whole brain. R_1 was negatively correlated with FC. Significant evidence indicates a link between cerebral myelin and FC, including a relationship between intracortical myelin and FC (Huntenburg et al., 2017; Wang et al., 2019); the prediction of cognition (Bells et al., 2017; Caeyenberghs et al., 2016) and FC-derived components (Messaritaki et al., 2021) using myelin-sensitive metrics; and a relationship between damaged myelin sheaths and greater conduction delays in multiple sclerosis (Sorrentino et al., 2022). At the cellular level, myelin contributes to conduction velocity (Huxley & Stämpfli, 1949), metabolic support (Nave & Werner, 2014), and plasticity (Gibson et al., 2018), all of which could be argued to support brain function. Myelin plasticity in particular can be described in terms of "activity-dependence," whereby an increase in the functional activity of a given circuit stimulates cellular signaling cascades, promoting greater myelination (Fields, 2015; Mount & Monje, 2017). Coupled with our results, this complex mix of functional roles supports the idea that structure-function models will be improved by integrating measures of myelin and connection strength.

An Opposing Relationship With Edge Length for Edge Caliber and Myelin Content

When controlling for edge length, we found an inverse relationship between R_1 and COMMIT over the whole brain in all subjects and at the group level. This suggests that the aggregate g-ratio (ratio of inner/outer diameters of myelinated axons) of a white matter tract may increase with edge caliber. At the cellular level, the diameter of an axon and the thickness of its myelin sheath show nearly a linear relationship over a broad range of smaller diameter axons; this relationship becomes increasingly nonlinear as axon diameter increases (Berthold et al., 1983; Hildebrand & Hahn, 1978). In general, increasing axon diameter tends to outpace increasing myelin thickness, that is, the g-ratio tends to increase with increasing axon caliber (Hildebrand & Hahn, 1978). Our findings suggest that this cellular-level principle may extend to the systems level: Increases in edge caliber tend to outpace changes in the myelin content, resulting in a concomitant increase in the g-ratio of white matter tracts.

We localized the inverse relationship between R_1 and COMMIT to the shortest edges, suggesting that the g-ratio was the highest in the shortest connections. This result is supported by a previous imaging study showing the highest g-ratio in "local" connections (Mancini et al., 2018). In general, we found that R_1 increased and COMMIT decreased with increasing edge length, which aligns with previously reported results of higher R_1 and fewer streamlines for the white matter connections between transmodal regions (Boshkovski et al., 2021). Both of these trends fit well with theories of brain wiring economy in which the energetic cost of maintaining biological material increases with connection length (Bullmore & Sporns, 2012). This natural pressure acts to reduce the total axonal volume of longer white matter bundles. Increasing the myelin content of longer tracts comes at a cost as well, but this may be at least partially offset as increasing myelin content reduces the total membrane surface area along which expensive electrochemical gradients must be maintained (Bullmore & Sporns, 2012). However, a cost-benefit analysis of the energetics of myelination concluded that the energetic cost of myelin

maintenance outweighs any savings on action potentials (Harris & Attwell, 2012). This suggests that higher myelination of longer edges may be better explained as a mechanism to provide trophic support (Nave & Werner, 2014) to vital interregional connections (van den Heuvel et al., 2012) or to reduce conduction delays.

Edge Weight Variance Decreases With Edge Length in Most Weighted Structural Networks

White matter features related to myelin content, connection strength, and neurite density tend to become more consistent across tracts as tract length increases. Greater variability in the weights of the shortest connections could result from a higher proportion of false positive streamlines influencing these edge weights. For SIFT2 and COMMIT, streamline weight computation becomes increasingly unstable with decreasing length as fewer voxels contribute to the fit. However, this result could also be explained more generally by contrasting the roles of shorter and longer connections in the brain. Shorter white matter tracts connect brain regions near each other in space, such as within the same module. Just as we might expect the characteristics of smaller roads and streets (e.g., width, building materials, markings, signs, sidewalks) to vary by neighborhood and city, we might also expect the morphology of shorter white matter connections to change as the functional specialization of any given region or module changes. On the other hand, longer tracts (i.e., the freeways of the brain) may overlap more in both their functional role and their morphological features relative to shorter connections, hence lower edge weight variability. Breaking with the above pattern, FA and RD showed the highest edge weight variance in the longest connections. Given that structural measures derived using a voxel-wise diffusion tensor model are particularly sensitive to the white matter "architectural paradigm" (Jones et al., 2013), these results suggest that white matter features related to fiber orientation and geometry actually diverge with increasing tract length. Note that we are unable to say decisively whether the edge weight variance measured in these structural and functional brain networks corresponds to true signal or noise. The inclusion of scan-rescan data (e.g., as in Amico & Goñi, 2018) could support stronger conclusions as to the source of this variability.

The Absence of a Rich Club in Structural Networks Weighted by R_1 and FA

Group-level R_1 and FA did not show a normalized weighted rich club for any degree k. Higher myelination in the white matter tracts connecting rich-club nodes has previously been reported (Collin et al., 2014); however, methodological differences limit comparability. A rich club has previously been reported in FA-weighted networks using similar methods to ours (van den Heuvel & Sporns, 2011). The source of this disagreement could potentially be attributed to differences in our tractography algorithm, parcellation, or null network computation.

In weighted rich-club detection, the identification of a densely connected core is independent of edge weight (depends only on node degree), but the designation of this subnetwork as a rich club requires that it contains a higher-than-chance proportion of the strongest edges from the full network. Indeed, this is the case over a broad range of degree k for COMMIT. Over the same range of k, the normalized rich-club curves for R_1 and FA are inverted about the threshold value of 1 with respect to COMMIT. This implies that the subnetwork found at a given k in this range contains edges that tend to show higher COMMIT and lower R_1 edge weights than expected by chance. We previously showed edgewise inverse correlations between R_1 and COMMIT that were robust to controlling for edge length. We also showed that R_1 and FA are positively correlated under these same conditions. In this light, it is not surprising that the edges connecting rich-club nodes tend to show opposite trends in R_1- and FA-weighting with respect to COMMIT. Nonetheless, it is possible that the lack of a rich

club in our myelin-weighted network is an artifact of tractometry. Future work will attempt to replicate this result using myelin-weighted networks computed with a different methodology (Schiavi et al., 2022).

Replication Across Parcellation Resolution and in a Second Dataset

In this report, we have chosen to feature data in the Schaefer-400 cortical parcellation plus 14 subcortical nodes. However, there is little consensus on the best brain atlas, and the optimal choice likely depends on the specifics of your data and the question being investigated. In a supplementary analysis, we replicated our results across 100- to 900-node Schaefer cortical atlases. We found that residual edgewise correlations with FC (Supporting Information Figure S1) and R_1 (Supporting Information Figure S2), as well as normalized rich club and normalized small-worldness (Supporting Information Figure S3), were robust to parcellation resolution. In contrast, the spatial topography of high-hubness brain regions appears qualitatively dependent on parcellation granularity, although further analyses would be necessary to draw stronger conclusions (Supporting Information Figure S4).

An independent multimodal dataset was also used to replicate the main SC results, including the residual edgewise correlations with R_1 and the relationship between R_1 and COMMIT across edge length bins (Supporting Information Figure S5), as well as all network topology results (Supporting Information Figure S6).

Limitations

Streamline tractography is known to suffer from several important biases, including both false positive and false negative streamlines, which can influence downstream analyses (Maier-Hein et al., 2017; Schilling et al., 2019; Sotiropoulos & Zalesky, 2019; Zalesky et al., 2016). Through probabilistic tractography, we opted to minimize false negatives while maximizing false positives. This allowed us to implement careful streamline- and edge-filtering strategies in postprocessing to address this known bias. Still, without a ground truth, we cannot quantify the extent to which we were successful in mitigating this issue, nor can we guarantee that we did not erroneously filter true positive streamlines or edges. All processing and filtering methods were consistent and network density was uniform across weighted structural networks. Thus, any major tractography bias should be as homogeneous as possible across networks.

Tractometry-derived brain networks suffer from widespread partial volume effects due to crossing and kissing fibers in a majority of white matter voxels. The net effect of this bias is well understood and is apparent in our results and previous work (De Santis et al., 2014; Schiavi et al., 2022). Nonetheless, this method was included here, as our goal was to characterize widely used structural connectivity methods. New techniques for reducing this bias are currently being developed; these techniques allow for the estimation of tract-specific microstructural features (e.g., Barakovic, Girard, et al., 2021; Barakovic, Tax, et al., 2021; De Santis et al., 2016; Leppert et al., 2021, 2023; Schiavi et al., 2022).

We were unable to assess repeatability in this work as we did not have scan-rescan data. However, reproducibility has already been assessed for NODDI (Chung et al., 2016; Lehmann et al., 2021), MP2RAGE-derived T1 maps (Marques et al., 2010), diffusion-tractography-based structural connectivity (Bonilha et al., 2015), as well as COMMIT and SIFT2 tractogram filtering (Koch et al., 2022). The reproducibility of the tractometry features (R_1, FA, RD, ICVF) will mainly depend on these previous steps and the accuracy of the spatial alignment of the multimodal data.

In this work, we have attempted to thoroughly examine the fundamental properties of a wide range of standard and state-of-the-art metrics for quantifying white matter brain structure. However, the scope of possible methods and their respective variants is too broad to treat thoroughly in a single body of work. In particular, track-weighted imaging (Calamante, 2017; Calamante et al., 2010, 2012) and fixel-based analysis (Dhollander et al., 2021; Raffelt et al., 2015, 2017) provide state-of-the-art solutions to the challenge of quantifying white matter structural features in the presence of crossing fibers.

Conclusion

We presented a thorough characterization of weighted SC networks. Overall, our findings support the joint use of SC networks weighted by connection strength and myelin in predicting FC. In particular, using the COMMIT or SIFT2 algorithms to quantify connection strength shows promise to improve model interpretability relative to NoS. Beyond R_1, there is a wide array of myelin-sensitive metrics that could be used to compute useful myelin-weighted networks. The integration of this microstructure-weighted connectivity approach into structure-function models will advance the mechanistic interpretation of both the function and the dysfunction of the living human brain.

MATERIALS AND METHODS

Data Acquisition and Preprocessing

Multimodal MRI data were collected in 50 healthy volunteers at 3 Tesla on a Siemens Magnetom Prisma-Fit scanner equipped with a 64-channel head coil as follows:

- T_1-weighted (T_1w) anatomical: 3D magnetization-prepared rapid gradient-echo sequence (MP-RAGE; 0.8 mm isotropic; TR = 2,300 ms; TE = 3.14 ms; TI = 900 ms; iPAT = 2; partial Fourier = 6/8).
- Multi-shell diffusion-weighted imaging (DWI): 2D pulsed gradient spin-echo echo-planar imaging sequence consisting of three shells with b-values 300, 700, and 2,000 s/mm^2 and diffusion directions 10, 40, and 90, respectively (1.6 mm isotropic; TR = 3,500 ms, TE = 64.40 ms; multiband factor = 3); b0 images were also acquired with reverse phase encoding direction to facilitate distortion correction of DWI data.
- 7 min of resting-state functional MRI: multiband accelerated 2D-BOLD gradient echo echo-planar sequence (3 mm isotropic; TR = 600 ms, TE = 30 ms; mb factor = 6; flip angle = 52°). Two spin-echo images with AP and PA phase encoding were additionally acquired (3 mm isotropic; TR = 4,029 ms; TE = 48 ms; flip angle = 90°).
- Quantitative T_1 relaxometry data were acquired with a 3D-MP2RAGE sequence (Marques et al., 2010) (0.8 mm isotropic; TR = 5,000 ms, TE = 2.9 ms, TI_1 = 940 ms, $T1_2$ = 2,830 ms; iPAT = 3; partial Fourier = 6/8). This was used to compute a T_1 map that was sampled to estimate the edge weights in R_1 ($1/T_1$) networks (myelin-weighted).

The multimodal processing pipeline *micapipe* (Cruces et al., 2022) (https://micapipe.readthedocs.io/) was used to preprocess diffusion, anatomical, and functional images. T_1w images were deobliqued, reoriented to standard neuroscience orientation (LPI), corrected for intensity nonuniformity (Tustison et al., 2010), intensity normalized, and skull stripped. Subcortical segmentations were performed with FSL FIRST (Jenkinson et al., 2012; Patenaude et al., 2011) and tissue types were classified using FSL FAST (Y. Zhang et al., 2001). A five-tissue-type image segmentation was generated for anatomically constrained tractography

(R. E. Smith et al., 2012). Cortical surface segmentations were generated with FreeSurfer 6.0 (Dale et al., 1999; Fischl, Sereno, & Dale, 1999; Fischl, Sereno, Tootell, & Dale, 1999).

Diffusion preprocessing was performed in native DWI space using tools from MRtrix3 (Tournier et al., 2012, 2019) and proceeded in the following sequence: (1) image denoising (Cordero-Grande et al., 2019; Veraart, Fieremans, et al., 2016; Veraart, Novikov, et al., 2016); (2) two b = 0 s/mm^2 volumes with reverse phase encoding were used to correct for susceptibility distortion, head motion, and eddy currents via FSL's eddy and TOPUP tools (Andersson et al., 2003; Andersson & Sotiropoulos, 2016; S. M. Smith et al., 2004); and (3) B1+ bias-field correction (Tustison et al., 2010). These preprocessed data were used to estimate multi-shell and multi-tissue response functions for constrained spherical-deconvolution (Christiaens et al., 2015; Dhollander et al., 2016, 2019; Jeurissen et al., 2014) followed by intensity normalization. Nonlinear registration was performed with ANTs (Avants et al., 2008) to coregister anatomical images to DWI space.

Resting-state fMRI preprocessing entailed discarding the first five TRs, reorientation (LPI), motion correction by registering all volumes to the mean, and distortion correction using main phase and reverse phase field maps. Nuisance signal was removed using an ICA-FIX (Salimi-Khorshidi et al., 2014) classifier and by spike regression using motion outlier outputs from FSL (Jenkinson et al., 2012). Volumetric time series were averaged for boundary-based registration (Greve & Fischl, 2009) to native FreeSurfer space and mapped to individual surfaces using trilinear interpolation. Spatial smoothing (Gaussian, FWHM = 10 mm) was applied to native-surface and template-mapped cortical time series.

Tractography and Microstructural Metrics

To estimate structural connectomes, anatomically constrained tractography (R. E. Smith et al., 2012) was performed on the normalized white matter FOD image using the probabilistic algorithm iFOD2 (Tournier et al., 2010). Tractograms of 5 million streamlines were generated by seeding the gray-white matter interface using the following parameters: max length = 400, min length = 10, angle = 22.5, step = 0.5, cutoff = 0.06, backtrack, crop_at_gmwmi (gray-matter-white-matter interface). These tractograms were filtered in a two-stage process: (1) A temporary whole-brain connectome weighted by NoS was computed then decomposed into its composite streamlines to derive a new tractogram in which any streamline that failed to connect two gray matter ROIs in the temporary connectome was excluded. This "streamline-filtering" step typically resulted in approximately a 5% decrease in the size of the tractogram (~250,000 streamlines removed) and was undertaken to ensure that these erroneous streamlines did not affect the COMMIT model. Streamline-filtered tractograms were used to compute NoS and were used as inputs to both the SIFT2 and the COMMIT models. COMMIT was run using a Stick-Zeppelin-Ball forward model and default settings (see https://github.com/daducci/COMMIT). (2) Any streamline with a COMMIT weight < 1e^{-12} (machine precision 0) was interpreted as a false positive and filtered from the tractogram. This streamline-level COMMIT-filtering step typically resulted in greater than a 90% decrease in the size of the tractogram, with most containing between ~300,000 and 600,000 streamlines. COMMIT-filtered tractograms were used not only in the computation of COMMIT, but in all tractometry networks as well. This additional filtering step was performed on COMMIT streamline weights only (not SIFT2) to reduce the impact of false positive streamlines in tractometry networks as much as possible.

In a supplemental analysis, the COMMIT streamline weights were additionally used in the computation of edge weights in tractometry-derived networks by performing a COMMIT-

weighted average of a given tractometry metric (e.g., FA) over streamlines for each node pair (Supporting Information Figures S10–S12).

Construction of Weighted Structural Networks

The streamline-specific SC networks were computed in the following manner: (1) NoS as the summed streamline count; (2) LoS as the mean streamline length; (3) SIFT2 as the sum of SIFT2 streamline weights; and (4) COMMIT as the length-weighted sum of COMMIT streamline weights as in Schiavi et al. (2020). Explicitly, edgewise entries in COMMIT-weighted networks were computed as the following:

$$\alpha_{ij} = \frac{\sum_{k=1}^{N_{ij}} \left(x_{ij}^{k} \times l_k \right)}{\bar{L}_{ij}},$$

where α_{ij} is the edge weight between nodes i and j; $\bar{L}_{ij}$ is the mean streamline length; N_{ij} is the number of streamlines; x_{ij}^{k} is the COMMIT weight of streamline k; and l_k is its length. Edge weights in NoS, SIFT2, and COMMIT were normalized by node volume.

SC networks weighted by FA, RD, ICVF (H. Zhang et al., 2012), and R_1 were derived using multimodal tractometry (Bells et al., 2011). Streamline weights were computed by (1) coregistering the tractogram and desired image and (2) sampling the voxel-level aggregate value along the length of each streamline. Edge weights were computed as the median along each streamline and the mean across streamlines by node pair. Voxel-wise measures of FA and RD were computed with a diffusion tensor model (Basser et al., 1994) and ICVF by applying the NODDI multicompartment model (H. Zhang et al., 2012) to preprocessed DWI data (Daducci, Canales-Rodríguez, et al., 2015).

The 400-node Schaefer (Schaefer et al., 2018) cortical parcellation is used in all results. Subcortical ROIs corresponded to 7 bilateral regions (14 nodes): amygdala, thalamus, caudate, accumbens, putamen, hippocampus, and pallidum. A single static, zero-lag FC network was derived by product-moment pairwise Pearson cross-correlation of node-averaged time series. FC network edge weights were Fisher Z-transformed.

Connectome Post-processing

COMMIT-weighted networks were used to filter all other weighted structural networks at the edge level. This was chosen as COMMIT-weighted networks had the lowest connection density to start, and all nonzero COMMIT edges were also nonzero in all other SC networks. All SC networks were thresholded at the edge level within subject by (1) setting edges = 0 in all weighted SC networks if that edge had a COMMIT weight < $1e^{-12}$ and (2) applying a 50% uniform threshold mask to facilitate group-consensus averaging. This minimized differences in binary structural network density across subjects and enforced a uniform binary connectivity map across weighted SC networks at the group level and within subject. Group-level networks were computed as the subject-wise mean at each edge excluding zero-valued edges.

Network Analysis

Network analysis was performed using tools (Rubinov & Sporns, 2010) based on graph theory (Fornito et al., 2013; Sporns, 2018). Measures of clustering coefficient and path length were normalized against 50 degree- and strength-preserving null networks. Clustering coefficient was normalized within node then averaged across nodes to obtain a scalar

value per network. The following weight (W_{ij}) to length (L_{ij}) transform was used in path length computation: $L_{ij} = -\log(W_{ij})$. Weighted rich-club curves were normalized against 1,000 degree- and strength-preserving null networks. The edges in all degree- and strength-preserving null networks were rewired $1e^6$ times total, and the strength sequence was approximated using simulated annealing. Rich-club curves were normalized in binary networks against 1,000 degree-preserving null networks in which each edge was rewired 100 times. All edge rewiring followed the Maslov-Sneppen rewiring model (Maslov & Sneppen, 2002). Similar to van den Heuvel et al. (2010), hubness scores (0–5) were computed as 1 point for all nodes showing top 20% strength, betweenness, closeness, or eigenvector centrality; and lowest 20% clustering coefficient.

Maslov-Sneppen rewiring: An iterative rewiring process used to randomize the connections of an empirical network while preserving network size, connection density, and degree distribution.

Permutation Testing

Statistical significance for the edgewise correlation of residual edge weights in NoS, SIFT2, COMMIT, and R_1 with FC (Supporting Information Figure S7), as well as all connection-strength-weighted networks with R_1 (Supporting Information Figure S8), was quantified using permutation testing as described in the Supporting Information. One-sided p values are reported in the main text figures as p_{perm}.

ACKNOWLEDGMENTS

Data collection at the McConnell Brain Imaging Centre was supported by Brain Canada and Healthy Brains for Healthy Lives.

DATA AVAILABILITY

These data are available for download (https://portal.conp.ca/dataset?id=projects/mica-mics; Royer et al., 2022b). See Royer et al. (2022a) and Cruces et al. (2022) for full details of data acquisition and processing. All data processing and analysis code is openly available at https://github.com/TardifLab/Weighted-SC-Networks (Nelson, 2023).

SUPPORTING INFORMATION

Supporting information for this article is available at https://doi.org/10.1162/netn_a_00330.

AUTHOR CONTRIBUTIONS

Mark Cameron Nelson: Conceptualization; Formal analysis; Methodology; Project administration; Software; Validation; Visualization; Writing – original draft; Writing – review & editing. Jessica Royer: Data curation; Software; Writing – review & editing. Wen Da Lu: Data curation; Methodology; Writing – review & editing. Ilana R. Leppert: Methodology; Writing – review & editing. Jennifer Campbell: Methodology; Writing – review & editing. Simona Schiavi: Methodology; Writing – review & editing. Hannah Jin: Conceptualization; Methodology; Writing – review & editing. Shahin Tavakol: Data curation. Reinder Vos de Wael: Data curation; Software. Raul Rodriguez-Cruces: Software. G. Bruce Pike: Writing – review & editing. Boris Bernhardt: Funding acquisition; Writing – review & editing. Alessandro Daducci: Methodology; Software; Writing – review & editing. Bratislav Misic: Conceptualization; Methodology; Supervision; Writing – review & editing. Christine Tardif: Conceptualization; Funding acquisition; Methodology; Project administration; Resources; Supervision; Writing – review & editing.

FUNDING INFORMATION

Boris Bernhardt, NSERC-Discovery, Award ID: 1304413, DGECR-2018-00216. Boris Bernhardt, CIHR, Award ID: FDN-154298, PJT-174995. Boris Bernhardt, SickKids New Investigator, Award ID: NI17-039. Boris Bernhardt, Azrieli Center for Autism Research, Montreal Neurological Institute. Boris Bernhardt, Brain Canada Azrieli Future Leaders. Boris Bernhardt, Tier-2 Canada Research Chairs program. Christine Tardif, Fonds de Recherche du Québec – Santé, Research Scholar Junior 1, Award ID: 280246 and 266479. Christine Tardif, Healthy Brains for Healthy Lives, Award ID: 1c-ll-13. Christine Tardif, NSERC-Discovery, Award ID: 1304413, RGPIN-2018-05176.

REFERENCES

Alexander, D. C., Dyrby, T. B., Nilsson, M., & Zhang, H. (2019). Imaging brain microstructure with diffusion MRI: Practicality and applications. *NMR in Biomedicine*, *32*(4), e3841. https://doi.org/10.1002/nbm.3841, PubMed: 29193413

Alexander, D. C., Hubbard, P. L., Hall, M. G., Moore, E. A., Ptito, M., Parker, G. J. M., & Dyrby, T. B. (2010). Orientationally invariant indices of axon diameter and density from diffusion MRI. *NeuroImage*, *52*(4), 1374–1389. https://doi.org/10.1016/j.neuroimage.2010.05.043, PubMed: 20580932

Amico, E., & Goñi, J. (2018). The quest for identifiability in human functional connectomes. *Scientific Reports*, *8*(1), 8254. https://doi.org/10.1038/s41598-018-25089-1, PubMed: 29844466

Andersson, J. L. R., Skare, S., & Ashburner, J. (2003). How to correct susceptibility distortions in spin-echo echo-planar images: Application to diffusion tensor imaging. *NeuroImage*, *20*(2), 870–888. https://doi.org/10.1016/S1053-8119(03)00336-7, PubMed: 14568458

Andersson, J. L. R., & Sotiropoulos, S. N. (2016). An integrated approach to correction for off-resonance effects and subject movement in diffusion MR imaging. *NeuroImage*, *125*, 1063–1078. https://doi.org/10.1016/j.neuroimage.2015.10.019, PubMed: 26481672

Assaf, Y., Blumenfeld-Katzir, T., Yovel, Y., & Basser, P. J. (2008). AxCaliber: A method for measuring axon diameter distribution from diffusion MRI. *Magnetic Resonance in Medicine*, *59*(6), 1347–1354. https://doi.org/10.1002/mrm.21577, PubMed: 18506799

Avants, B. B., Epstein, C. L., Grossman, M., & Gee, J. C. (2008). Symmetric diffeomorphic image registration with cross-correlation: Evaluating automated labeling of elderly and neurodegenerative brain. *Medical Image Analysis*, *12*(1), 26–41. https://doi.org/10.1016/j.media.2007.06.004, PubMed: 17659998

Barakovic, M., Girard, G., Schiavi, S., Romascano, D., Descoteaux, M., Granziera, C., Jones, D. K., Innocenti, G. M., Thiran, J.-P., & Daducci, A. (2021). Bundle-specific axon diameter index as a new contrast to differentiate white matter tracts. *Frontiers in Neuroscience*, *15*, 646034. https://doi.org/10.3389/fnins.2021.646034, PubMed: 34211362

Barakovic, M., Tax, C. M. W., Rudrapatna, U., Chamberland, M., Rafael-Patino, J., Granziera, C., Thiran, J. P., Daducci, A., Canales-Rodríguez, E. J., & Jones, D. K. (2021). Resolving bundle-specific intra-axonal T2 values within a voxel using diffusion-relaxation tract-based estimation. *NeuroImage*, *227*, 117617. https://doi.org/10.1016/j.neuroimage.2020.117617, PubMed: 33301934

Basser, P. J. (1995). Inferring microstructural features and the physiological state of tissues from diffusion-weighted images. *NMR in Biomedicine*, *8*(7), 333–344. https://doi.org/10.1002/nbm.1940080707, PubMed: 8739270

Basser, P. J., Mattiello, J., & LeBihan, D. (1994). Estimation of the effective self-diffusion tensor from the NMR spin echo. *Journal of Magnetic Resonance, Series B*, *103*(3), 247–254. https://doi.org/10.1006/jmrb.1994.1037, PubMed: 8019776

Bassett, D. S., & Bullmore, E. (2006). Small-world brain networks. *Neuroscientist*, *12*(6), 512–523. https://doi.org/10.1177/1073858406293182, PubMed: 17079517

Bassett, D. S., & Bullmore, E. T. (2017). Small-world brain networks revisited. *Neuroscientist*, *23*(5), 499–516. https://doi.org/10.1177/1073858416667720, PubMed: 27655008

Bells, S., Cercignani, M., Deoni, S., & Assaf, Y. (2011). "Tractometry"—Comprehensive multi-modal quantitative assessment of white matter along specific tracts. *Proceedings of the International Society for Magnetic Resonance in Medicine*, *19*(2009), 678. https://cds.ismrm.org/protected/11MProceedings/PDFfiles/678.pdf

Bells, S., Lefebvre, J., Prescott, S. A., Dockstader, C., Bouffet, E., Skocic, J., Laughlin, S., & Mabbott, D. J. (2017). Changes in white matter microstructure impact cognition by disrupting the ability of neural assemblies to synchronize. *Journal of Neuroscience*, *37*(34), 8227–8238. https://doi.org/10.1523/JNEUROSCI.0560-17.2017, PubMed: 28743724

Berthold, C. H., Nilsson, I., & Rydmark, M. (1983). Axon diameter and myelin sheath thickness in nerve fibres of the ventral spinal root of the seventh lumbar nerve of the adult and developing cat. *Journal of Anatomy*, *136*(Pt. 3), 483–508. PubMed: 6885614

Biswal, B., Zerrin Yetkin, F., Haughton, V. M., & Hyde, J. S. (1995). Functional connectivity in the motor cortex of resting human brain using echo-planar MRI. *Magnetic Resonance in Medicine*, *34*(4), 537–541. https://doi.org/10.1002/mrm.1910340409, PubMed: 8524021

Bonilha, L., Gleichgerrcht, E., Fridriksson, J., Breedlove, J. L., Rorden, C., Nesland, T., Paulus, W., Helms, G., & Focke, N. K. (2015).

Reproducibility of the structural brain connectome derived from diffusion tensor imaging. *PLOS ONE*, *10*(9), e0135247. https://doi.org/10.1371/journal.pone.0135247, PubMed: 26332788

Boshkovski, T., Kocarev, L., Cohen-Adad, J., Mišić, B., Lehéricy, S., Stikov, N., & Mancini, M. (2021). The R1-weighted connectome: Complementing brain networks with a myelin-sensitive measure. *Network Neuroscience*, *5*(2), 358–372. https://doi.org/10.1162/netn_a_00179, PubMed: 34189369

Bullmore, E., & Sporns, O. (2012). The economy of brain network organization. *Nature Reviews Neuroscience*, *13*(5), 336–349. https://doi.org/10.1038/nrn3214, PubMed: 22498897

Cabral, J., Kringelbach, M. L., & Deco, G. (2017). Functional connectivity dynamically evolves on multiple time-scales over a static structural connectome: Models and mechanisms. *NeuroImage*, *160*, 84–96. https://doi.org/10.1016/j.neuroimage.2017.03.045, PubMed: 28343985

Caeyenberghs, K., Metzler-Baddeley, C., Foley, S., & Jones, D. K. (2016). Dynamics of the human structural connectome underlying working memory training. *Journal of Neuroscience*, *36*(14), 4056–4066. https://doi.org/10.1523/JNEUROSCI.1973-15.2016, PubMed: 27053212

Calamante, F. (2017). Track-weighted imaging methods: Extracting information from a streamlines tractogram. *Magnetic Resonance Materials in Physics, Biology and Medicine*, *30*(4), 317–335. https://doi.org/10.1007/s10334-017-0608-1, PubMed: 28181027

Calamante, F., Tournier, J. D., Jackson, G. D., & Connelly, A. (2010). Track-density imaging (TDI): Super-resolution white matter imaging using whole-brain track-density mapping. *NeuroImage*, *53*(4), 1233–1243. https://doi.org/10.1016/j.neuroimage.2010.07.024, PubMed: 20643215

Calamante, F., Tournier, J. D., Smith, R. E., & Connelly, A. (2012). A generalised framework for super-resolution track-weighted imaging. *NeuroImage*, *59*(3), 2494–2503. https://doi.org/10.1016/j.neuroimage.2011.08.099, PubMed: 21925280

Christiaens, D., Reisert, M., Dhollander, T., Sunaert, S., Suetens, P., & Maes, F. (2015). Global tractography of multi-shell diffusion-weighted imaging data using a multi-tissue model. *NeuroImage*, *123*, 89–101. https://doi.org/10.1016/j.neuroimage.2015.08.008, PubMed: 26272729

Chung, A. W., Seunarine, K. K., & Clark, C. A. (2016). NODDI reproducibility and variability with magnetic field strength: A comparison between 1.5 T and 3 T. *Human Brain Mapping*, *37*(12), 4550–4565. https://doi.org/10.1002/hbm.23328, PubMed: 27477113

Collin, G., Sporns, O., Mandl, R. C. W., & van den Heuvel, M. P. (2014). Structural and functional aspects relating to cost and benefit of rich club organization in the human cerebral cortex. *Cerebral Cortex*, *24*(9), 2258–2267. https://doi.org/10.1093/cercor/bht064, PubMed: 23551922

Cordero-Grande, L., Christiaens, D., Hutter, J., Price, A. N., & Hajnal, J. V. (2019). Complex diffusion-weighted image estimation via matrix recovery under general noise models. *NeuroImage*, *200*, 391–404. https://doi.org/10.1016/j.neuroimage.2019.06.039, PubMed: 31226495

Cruces, R. R., Royer, J., Herholz, P., Larivière, S., Vos de Wael, R., Paquola, C., Benkarim, O., Park, B.-Y., Degré-Pelletier, J., Nelson, M. C., DeKraker, J., Leppert, I. R., Tardif, C., Poline, J.-B., Concha, L., & Bernhardt, B. C. (2022). Micapipe: A pipeline for multimodal neuroimaging and connectome analysis. *NeuroImage*, *263*, 119612. https://doi.org/10.1016/j.neuroimage.2022.119612, PubMed: 36070839

Daducci, A., Canales-Rodríguez, E. J., Zhang, H., Dyrby, T. B., Alexander, D. C., & Thiran, J. P. (2015). Accelerated Microstructure Imaging via Convex Optimization (AMICO) from diffusion MRI data. *NeuroImage*, *105*, 32–44. https://doi.org/10.1016/j.neuroimage.2014.10.026, PubMed: 25462697

Daducci, A., Dal Palù, A., Lemkaddem, A., & Thiran, J.-P. (2013). A convex optimization framework for global tractography. In *Proceedings of the 10th International Symposium on Biomedical Imaging* (pp. 524–527). IEEE. https://doi.org/10.1109/ISBI.2013.6556527

Daducci, A., Dal Palù, A., Lemkaddem, A., & Thiran, J. P. (2015). COMMIT: Convex optimization modeling for microstructure informed tractography. *IEEE Transactions on Medical Imaging*, *34*(1), 246–257. https://doi.org/10.1109/TMI.2014.2352414, PubMed: 25167548

Dale, A. M., Fischl, B., & Sereno, M. I. (1999). Cortical surface-based analysis. I. Segmentation and surface reconstruction. *NeuroImage*, *9*(2), 179–194. https://doi.org/10.1006/nimg.1998.0395, PubMed: 9931268

de Reus, M. A., & van den Heuvel, M. P. (2014). Simulated rich club lesioning in brain networks: A scaffold for communication and integration? *Frontiers in Human Neuroscience*, *8*, 647. https://doi.org/10.3389/fnhum.2014.00647, PubMed: 25191259

De Santis, S., Assaf, Y., Jeurissen, B., Jones, D. K., & Roebroeck, A. (2016). T1 relaxometry of crossing fibres in the human brain. *NeuroImage*, *141*, 133–142. https://doi.org/10.1016/j.neuroimage.2016.07.037, PubMed: 27444568

De Santis, S., Drakesmith, M., Bells, S., Assaf, Y., & Jones, D. K. (2014). Why diffusion tensor MRI does well only some of the time: Variance and covariance of white matter tissue microstructure attributes in the living human brain. *NeuroImage*, *89*, 35–44. https://doi.org/10.1016/j.neuroimage.2013.12.003, PubMed: 24342225

Deligianni, F., Carmichael, D. W., Zhang, G. H., Clark, C. A., & Clayden, J. D. (2016). NODDI and tensor-based microstructural indices as predictors of functional connectivity. *PLOS ONE*, *11*(4), e0153404. https://doi.org/10.1371/journal.pone.0153404, PubMed: 27078862

Dhollander, T., Clemente, A., Singh, M., Boonstra, F., Civier, O., Duque, J. D., Egorova, N., Enticott, P., Fuelscher, I., Gajamange, S., Genc, S., Gottlieb, E., Hyde, C., Imms, P., Kelly, C., Kirkovski, M., Kolbe, S., Liang, X., Malhotra, A., … Caeyenberghs, K. (2021). Fixel-based analysis of diffusion MRI: Methods, applications, challenges and opportunities. *NeuroImage*, *241*, 118417. https://doi.org/10.1016/j.neuroimage.2021.118417, PubMed: 34298083

Dhollander, T., Mito, R., Raffelt, D., & Connelly, A. (2019). Improved white matter response function estimation for 3-tissue constrained spherical deconvolution. *Proceedings of the International Society of Magnetic Resonance in Medicine*, *27*, 555. https://www.researchgate.net/publication/331165168_Improved_white_matter_response_function_estimation_for_3-tissue_constrained_spherical_deconvolution

Dhollander, T., Raffelt, D., & Connelly, A. (2016). Unsupervised 3-tissue response function estimation from single-shell or multi-shell diffusion MR data without a co-registered T1 image. *ISMRM Workshop on Breaking the Barriers of Diffusion MRI*, *35*, 1–2. https://www.researchgate.net/publication/307863133

Drakesmith, M., Harms, R., Rudrapatna, S. U., Parker, G. D., Evans, C. J., & Jones, D. K. (2019). Estimating axon conduction velocity in vivo from microstructural MRI. *NeuroImage*, *203*, 116186. https://doi.org/10.1016/j.neuroimage.2019.116186, PubMed: 31542512

Fields, R. D. (2015). A new mechanism of nervous system plasticity: Activity-dependent myelination. *Nature Reviews Neuroscience*, *16*(12), 756–767. https://doi.org/10.1038/nrn4023, PubMed: 26585800

Finn, E. S., Huber, L., Jangraw, D. C., Molfese, P. J., & Bandettini, P. A. (2019). Layer-dependent activity in human prefrontal cortex during working memory. *Nature Neuroscience*, *22*(10), 1687–1695. https://doi.org/10.1038/s41593-019-0487-z, PubMed: 31551596

Fischl, B., Sereno, M. I., & Dale, A. M. (1999). Cortical surface-based analysis: II. Inflation, flattening, and a surface-based coordinate system. *NeuroImage*, *9*(2), 195–207. https://doi.org/10.1006/nimg.1998.0396, PubMed: 9931269

Fischl, B., Sereno, M. I., Tootell, R. B. H., & Dale, A. M. (1999). High-resolution intersubject averaging and a coordinate system for the cortical surface. *Human Brain Mapping*, *8*(4), 272–284. https://doi.org/10.1002/(SICI)1097-0193(1999)8:4<272::AID-HBM10>3.0.CO;2-4, PubMed: 10619420

Fornito, A., Zalesky, A., & Breakspear, M. (2013). Graph analysis of the human connectome: Promise, progress, and pitfalls. *NeuroImage*, *80*, 426–444. https://doi.org/10.1016/j.neuroimage.2013.04.087, PubMed: 23643999

Fornito, A., Zalesky, A., & Breakspear, M. (2015). The connectomics of brain disorders. *Nature Reviews Neuroscience*, *16*(3), 159–172. https://doi.org/10.1038/nrn3901, PubMed: 25697159

Fornito, A., Zalesky, A., & Bullmore, E. T. (2016). *Fundamentals of brain network analysis*. Elsevier. https://doi.org/10.1016/C2012-0-06036-X

Frigo, M., Deslauriers-Gauthier, S., Parker, D., Ismail, A. A. O., Kim, J. J., Verma, R., & Deriche, R. (2020). Diffusion MRI tractography filtering techniques change the topology of structural connectomes. *Journal of Neural Engineering*, *17*(6), 065002. https://doi.org/10.1088/1741-2552/abc29b, PubMed: 33075758

Friston, K. J. (2011). Functional and effective connectivity: A review. *Brain Connectivity*, *1*(1), 13–36. https://doi.org/10.1089/brain.2011.0008, PubMed: 22432952

Gibson, E. M., Geraghty, A. C., & Monje, M. (2018). Bad wrap: Myelin and myelin plasticity in health and disease. *Developmental Neurobiology*, *78*(2), 123–135. https://doi.org/10.1002/dneu.22541, PubMed: 28986960

Girard, G., Whittingstall, K., Deriche, R., & Descoteaux, M. (2014). Towards quantitative connectivity analysis: Reducing tractography biases. *NeuroImage*, *98*, 266–278. https://doi.org/10.1016/j.neuroimage.2014.04.074, PubMed: 24816531

Gordon, E. M., Laumann, T. O., Gilmore, A. W., Newbold, D. J., Greene, D. J., Berg, J. J., Ortega, M., Hoyt-Drazen, C., Gratton, C., Sun, H., Hampton, J. M., Coalson, R. S., Nguyen, A. L., McDermott, K. B., Shimony, J. S., Snyder, A. Z., Schlaggar, B. L., Petersen, S. E., Nelson, S. M., & Dosenbach, N. U. F. (2017). Precision functional mapping of individual human brains. *Neuron*, *95*(4), 791–807. https://doi.org/10.1016/j.neuron.2017.07.011, PubMed: 28757305

Greicius, M. D., Krasnow, B., Reiss, A. L., & Menon, V. (2003). Functional connectivity in the resting brain: A network analysis of the default mode hypothesis. *Proceedings of the National Academy of Sciences*, *100*(1), 253–258. https://doi.org/10.1073/pnas.0135058100, PubMed: 12506194

Greve, D. N., & Fischl, B. (2009). Accurate and robust brain image alignment using boundary-based registration. *NeuroImage*, *48*(1), 63–72. https://doi.org/10.1016/j.neuroimage.2009.06.060, PubMed: 19573611

Griffa, A., & van den Heuvel, M. P. (2018). Rich-club neurocircuitry: Function, evolution, and vulnerability. *Dialogues in Clinical Neuroscience*, *20*(2), 121–132. https://doi.org/10.31887/DCNS.2018.20.2/agriffa, PubMed: 30250389

Hampson, M., Driesen, N. R., Skudlarski, P., Gore, J. C., & Constable, R. T. (2006). Brain connectivity related to working memory performance. *Journal of Neuroscience*, *26*(51), 13338–13343. https://doi.org/10.1523/JNEUROSCI.3408-06.2006, PubMed: 17182784

Harris, J. J., & Attwell, D. (2012). The energetics of CNS white matter. *Journal of Neuroscience*, *32*(1), 356–371. https://doi.org/10.1523/JNEUROSCI.3430-11.2012, PubMed: 22219296

Heath, F., Hurley, S. A., Johansen-Berg, H., & Sampaio-Baptista, C. (2018). Advances in noninvasive myelin imaging. *Developmental Neurobiology*, *78*(2), 136–151. https://doi.org/10.1002/dneu.22552, PubMed: 29082667

Hildebrand, C., & Hahn, R. (1978). Relation between myelin sheath thickness and axon size in spinal cord white matter of some vertebrate species. *Journal of the Neurological Sciences*, *38*(3), 421–434. https://doi.org/10.1016/0022-510X(78)90147-8, PubMed: 310448

Hodgkin, A. L., & Huxley, A. F. (1952). A quantitative description of membrane current and its application to conduction and excitation in nerve. *Journal of Physiology*, *117*(4), 500–544. https://doi.org/10.1113/jphysiol.1952.sp004764, PubMed: 12991237

Honey, C. J., Sporns, O., Cammoun, L., Gigandet, X., Thiran, J. P., Meuli, R., & Hagmann, P. (2009). Predicting human resting-state functional connectivity from structural connectivity. *Proceedings of the National Academy of Sciences*, *106*(6), 2035–2040. https://doi.org/10.1073/pnas.0811168106, PubMed: 19188601

Huntenburg, J. M., Bazin, P. L., Goulas, A., Tardif, C. L., Villringer, A., & Margulies, D. S. (2017). A systematic relationship between functional connectivity and intracortical myelin in the human cerebral cortex. *Cerebral Cortex*, *27*(2), 981–997. https://doi.org/10.1093/cercor/bhx030, PubMed: 28184415

Huxley, A. F., & Stämpfli, R. (1949). Evidence for saltatory conduction in peripheral myelinated nerve fibres. *Journal of Physiology*, *108*(3), 315–339. https://doi.org/10.1113/jphysiol.1949.sp004335, PubMed: 16991863

Jenkinson, M., Beckmann, C. F., Behrens, T. E. J., Woolrich, M. W., & Smith, S. M. (2012). FSL. *NeuroImage*, *62*(2), 782–790. https://doi.org/10.1016/j.neuroimage.2011.09.015, PubMed: 21979382

Jeurissen, B., Descoteaux, M., Mori, S., & Leemans, A. (2019). Diffusion MRI fiber tractography of the brain. *NMR in Biomedicine*,

32(4), e3785. https://doi.org/10.1002/nbm.3785, PubMed: 28945294

Jeurissen, B., Leemans, A., Tournier, J. D., Jones, D. K., & Sijbers, J. (2012). Investigating the prevalence of complex fiber configurations in white matter tissue with diffusion magnetic resonance imaging. *Human Brain Mapping*, *34*(11), 2747–2766. https://doi.org/10.1002/hbm.22099, PubMed: 22611035

Jeurissen, B., Tournier, J. D., Dhollander, T., Connelly, A., & Sijbers, J. (2014). Multi-tissue constrained spherical deconvolution for improved analysis of multi-shell diffusion MRI data. *NeuroImage*, *103*, 411–426. https://doi.org/10.1016/j.neuroimage.2014.07.061, PubMed: 25109526

Jones, D. K. (2010). Challenges and limitations of quantifying brain connectivity in vivo with diffusion MRI. *Imaging in Medicine*, *2*(3), 341–355. https://doi.org/10.2217/iim.10.21

Jones, D. K., Knösche, T. R., & Turner, R. (2013). White matter integrity, fiber count, and other fallacies: The do's and don'ts of diffusion MRI. *NeuroImage*, *73*, 239–254. https://doi.org/10.1016/j.neuroimage.2012.06.081, PubMed: 22846632

Kim, D.-J., & Min, B.-K. (2020). Rich-club in the brain's macrostructure: Insights from graph theoretical analysis. *Computational and Structural Biotechnology Journal*, *18*, 1761–1773. https://doi.org/10.1016/j.csbj.2020.06.039, PubMed: 32695269

Koch, P. J., Girard, G., Brügger, J., Cadic-Melchior, A. G., Beanato, E., Park, C.-H., Morishita, T., Wessel, M. J., Pizzolato, M., Canales-Rodríguez, E. J., Fischi-Gomez, E., Schiavi, S., Daducci, A., Piredda, G. F., Hilbert, T., Kober, T., Thiran, J.-P., & Hummel, F. C. (2022). Evaluating reproducibility and subject-specificity of microstructure-informed connectivity. *NeuroImage*, *258*, 119356. https://doi.org/10.1016/j.neuroimage.2022.119356, PubMed: 35659995

Larivière, S., Paquola, C., Park, B., Royer, J., Wang, Y., Benkarim, O., Vos de Wael, R., Valk, S. L., Thomopoulos, S. I., Kirschner, M., Lewis, L. B., Evans, A. C., Sisodiya, S. M., McDonald, C. R., Thompson, P. M., & Bernhardt, B. C. (2021). The ENIGMA toolbox: Multiscale neural contextualization of multisite neuroimaging datasets. *Nature Methods*, *18*(7), 698–700. https://doi.org/10.1038/s41592-021-01186-4, PubMed: 34194050

Lehmann, N., Aye, N., Kaufmann, J., Heinze, H. J., Düzel, E., Ziegler, G., & Taubert, M. (2021). Longitudinal reproducibility of neurite orientation dispersion and density imaging (NODDI) derived metrics in the white matter. *Neuroscience*, *457*, 165–185. https://doi.org/10.1016/j.neuroscience.2021.01.005, PubMed: 33465411

Leppert, I. R., Andrews, D. A., Campbell, J. S. W., Park, D. J., Pike, G. B., Polimeni, J. R., & Tardif, C. L. (2021). Efficient whole-brain tract-specific T1 mapping at 3T with slice-shuffled inversion-recovery diffusion-weighted imaging. *Magnetic Resonance in Medicine*, *86*(2), 738–753. https://doi.org/10.1002/mrm.28734, PubMed: 33749017

Leppert, I. R., Bontempi, P., Rowley, C. D., Campbell, J. S., Nelson, M. C., Schiavi, S., Pike, G. B., Daducci, A., & Tardif, C. L. (2023). Dual-encoded magnetization transfer and diffusion imaging and its application to tract-specific microstructure mapping. *arXiv:2303.03449*. https://doi.org/10.48550/arXiv.2303.03449

Liégeois, R., Li, J., Kong, R., Orban, C., Van De Ville, D., Ge, T., Sabuncu, M. R., & Yeo, B. T. T. (2019). Resting brain dynamics at different timescales capture distinct aspects of human behavior. *Nature Communications*, *10*(1), 2317. https://doi.org/10.1038/s41467-019-10317-7, PubMed: 31127095

Liu, Z. Q., Vázquez-Rodríguez, B., Spreng, R. N., Bernhardt, B. C., Betzel, R. F., & Misic, B. (2022). Time-resolved structure-function coupling in brain networks. *Communications Biology*, *5*(1), 532. https://doi.org/10.1038/s42003-022-03466-x, PubMed: 35654886

Maier-Hein, K. H., Neher, P. F., Houde, J.-C., Côté, M.-A., Garyfallidis, E., Zhong, J., Chamberland, M., Yeh, F.-C., Lin, Y.-C., Ji, Q., Reddick, W. E., Glass, J. O., Chen, D. Q., Feng, Y., Gao, C., Wu, Y., Ma, J., Renjie, H., Li, Q., … Descoteaux, M. (2017). The challenge of mapping the human connectome based on diffusion tractography. *Nature Communications*, *8*(1), 1349. https://doi.org/10.1038/s41467-017-01285-x, PubMed: 29116093

Mancini, M., Giulietti, G., Dowell, N., Spanò, B., Harrison, N., Bozzali, M., & Cercignani, M. (2018). Introducing axonal myelination in connectomics: A preliminary analysis of g-ratio distribution in healthy subjects. *NeuroImage*, *182*, 351–359. https://doi.org/10.1016/j.neuroimage.2017.09.018, PubMed: 28917698

Mancini, M., Karakuzu, A., Cohen-Adad, J., Cercignani, M., Nichols, T. E., & Stikov, N. (2020). An interactive meta-analysis of MRI biomarkers of myelin. *eLife*, *9*, e61523. https://doi.org/10.7554/eLife.61523, PubMed: 33084576

Margulies, D. S., Ghosh, S. S., Goulas, A., Falkiewicz, M., Huntenburg, J. M., Langs, G., Bezgin, G., Eickhoff, S. B., Castellanos, F. X., Petrides, M., Jefferies, E., & Smallwood, J. (2016). Situating the default-mode network along a principal gradient of macroscale cortical organization. *Proceedings of the National Academy of Sciences*, *113*(44), 12574–12579. https://doi.org/10.1073/pnas.1608282113, PubMed: 27791099

Marques, J. P., Kober, T., Krueger, G., van der Zwaag, W., Van de Moortele, P. F., & Gruetter, R. (2010). MP2RAGE, a self bias-field corrected sequence for improved segmentation and T1-mapping at high field. *NeuroImage*, *49*(2), 1271–1281. https://doi.org/10.1016/j.neuroimage.2009.10.002, PubMed: 19819338

Maslov, S., & Sneppen, K. (2002). Specificity and stability in topology of protein networks. *Science*, *296*(5569), 910–913. https://doi.org/10.1126/science.1065103, PubMed: 11988575

Messaritaki, E., Foley, S., Schiavi, S., Magazzini, L., Routley, B., Jones, D. K., & Singh, K. D. (2021). Predicting MEG resting-state functional connectivity from microstructural information. *Network Neuroscience*, *5*(2), 477–504. https://doi.org/10.1162/netn_a_00187, PubMed: 34189374

Moore, S., Meschkat, M., Ruhwedel, T., Trevisiol, A., Tzvetanova, I. D., Battefeld, A., Kusch, K., Kole, M. H. P., Strenzke, N., Möbius, W., de Hoz, L., & Nave, K.-A. (2020). A role of oligodendrocytes in information processing. *Nature Communications*, *11*(1), 5497. https://doi.org/10.1038/s41467-020-19152-7, PubMed: 33127910

Mottershead, J. P., Schmierer, K., Clemence, M., Thornton, J. S., Scaravilli, F., Barker, G. J., Tofts, P. S., Newcombe, J., Cuzner, M. L., Ordidge, R. J., McDonald, W. I., & Miller, D. H. (2003). High field MRI correlates of myelin content and axonal density in multiple sclerosis: A post-mortem study of the spinal cord. *Journal of Neurology*, *250*(11), 1293–1301. https://doi.org/10.1007/s00415-003-0192-3, PubMed: 14648144

Mount, C. W., & Monje, M. (2017). Wrapped to adapt: Experience-dependent myelination. *Neuron*, *95*(4), 743–756. https://doi.org/10.1016/j.neuron.2017.07.009, PubMed: 28817797

Nave, K.-A., & Werner, H. B. (2014). Myelination of the nervous system: Mechanisms and functions. *Annual Review of Cell and Developmental Biology*, *30*, 503–533. https://doi.org/10.1146/annurev-cellbio-100913-013101, PubMed: 25288117

Nelson, M. C. (2023). Weighted SC networks, GitHub. https://github.com/TardifLab/Weighted-SC-Networks

Patenaude, B., Smith, S. M., Kennedy, D. N., & Jenkinson, M. (2011). A Bayesian model of shape and appearance for subcortical brain segmentation. *NeuroImage*, *56*(3), 907–922. https://doi.org/10.1016/j.neuroimage.2011.02.046, PubMed: 21352927

Pumphrey, R. J., & Young, J. Z. (1938). The rates of conduction of nerve fibres of various diameters in cephalopods. *Journal of Experimental Biology*, *15*(4), 453–466. https://doi.org/10.1242/jeb.15.4.453

Raffelt, D., Smith, R., Ridgway, G., Tournier, J. D., Vaughan, D., Rose, S., Henderson, R., & Connelly, A. (2015). Connectivity-based fixel enhancement: Whole-brain statistical analysis of diffusion MRI measures in the presence of crossing fibres. *NeuroImage*, *117*, 40–55. https://doi.org/10.1016/j.neuroimage.2015.05.039, PubMed: 26004503

Raffelt, D., Tournier, J. D., Smith, R., Vaughan, D., Jackson, G., Ridgway, G., & Connelly, A. (2017). Investigating white matter fibre density and morphology using fixel-based analysis. *NeuroImage*, *144*, 58–73. https://doi.org/10.1016/j.neuroimage.2016.09.029, PubMed: 27639350

Royer, J., Rodríguez-Cruces, R., Tavakol, S., Larivière, S., Herholz, P., Li, Q., Vos de Wael, R., Paquola, C., Benkarim, O., Park, B., Lowe, A. J., Margulies, D., Smallwood, J., Bernasconi, A., Bernasconi, N., Frauscher, B., & Bernhardt, B. C. (2022a). An open MRI dataset for multiscale neuroscience. *Scientific Data*, *9*(1), 569. https://doi.org/10.1038/s41597-022-01682-y, PubMed: 36109562

Royer, J., Rodríguez-Cruces, R., Tavakol, S., Larivière, S., Herholz, P., Li, Q., Vos de Wael, R., Paquola, C., Benkarim, O., Park, B., Lowe, A. J., Margulies, D., Smallwood, J., Bernasconi, A., Bernasconi, N., Frauscher, B., & Bernhardt, B. C. (2022b). *MICA-MICs: A dataset for microstructure-informed connectomics* [Data set]. https://portal.conp.ca/dataset?id=projects/mica-mics

Rubinov, M., & Sporns, O. (2010). Complex network measures of brain connectivity: Uses and interpretations. *NeuroImage*, *52*(3), 1059–1069. https://doi.org/10.1016/j.neuroimage.2009.10.003, PubMed: 19819337

Salimi-Khorshidi, G., Douaud, G., Beckmann, C. F., Glasser, M. F., Griffanti, L., & Smith, S. M. (2014). Automatic denoising of functional MRI data: Combining independent component analysis and hierarchical fusion of classifiers. *NeuroImage*, *90*, 449–468. https://doi.org/10.1016/j.neuroimage.2013.11.046, PubMed: 24389422

Schaefer, A., Kong, R., Gordon, E. M., Laumann, T. O., Zuo, X.-N., Holmes, A. J., Eickhoff, S. B., & Yeo, B. T. T. (2018). Local-global parcellation of the human cerebral cortex from intrinsic functional connectivity MRI. *Cerebral Cortex*, *28*(9), 3095–3114. https://doi.org/10.1093/cercor/bhx179, PubMed: 28981612

Schiavi, S., Lu, P., Weigel, M., Lutti, A., Jones, D. K., Kappos, L., Granziera, C., & Daducci, A. (2022). Bundle myelin fraction (BMF) mapping of different white matter connections using microstructure informed tractography. *NeuroImage*, *249*, 118922. https://doi.org/10.1016/j.neuroimage.2022.118922, PubMed: 35063648

Schiavi, S., Petracca, M., Battocchio, M., El Mendili, M. M., Paduri, S., Fleysher, L., Inglese, M., & Daducci, A. (2020). Sensory-motor network topology in multiple sclerosis: Structural connectivity analysis accounting for intrinsic density discrepancy. *Human Brain Mapping*, *41*(11), 2951–2963. https://doi.org/10.1002/hbm.24989, PubMed: 32412678

Schilling, K. G., Daducci, A., Maier-Hein, K., Poupon, C., Houde, J. C., Nath, V., Anderson, A. W., Landman, B. A., & Descoteaux, M. (2019). Challenges in diffusion MRI tractography—Lessons learned from international benchmark competitions. *Magnetic Resonance Imaging*, *57*, 194–209. https://doi.org/10.1016/j.mri.2018.11.014, PubMed: 30503948

Smith, R. E., Tournier, J. D., Calamante, F., & Connelly, A. (2012). Anatomically-constrained tractography: Improved diffusion MRI streamlines tractography through effective use of anatomical information. *NeuroImage*, *62*(3), 1924–1938. https://doi.org/10.1016/j.neuroimage.2012.06.005, PubMed: 22705374

Smith, R. E., Tournier, J. D., Calamante, F., & Connelly, A. (2015). SIFT2: Enabling dense quantitative assessment of brain white matter connectivity using streamlines tractography. *NeuroImage*, *119*, 338–351. https://doi.org/10.1016/j.neuroimage.2015.06.092, PubMed: 26163802

Smith, S. M., Fox, P. T., Miller, K. L., Glahn, D. C., Fox, P. M., Mackay, C. E., Filippini, N., Watkins, K. E., Toro, R., Laird, A. R., & Beckmann, C. F. (2009). Correspondence of the brain's functional architecture during activation and rest. *Proceedings of the National Academy of Sciences*, *106*(31), 13040–13045. https://doi.org/10.1073/pnas.0905267106, PubMed: 19620724

Smith, S. M., Jenkinson, M., Woolrich, M. W., Beckmann, C. F., Behrens, T. E. J., Johansen-Berg, H., Bannister, P. R., De Luca, M., Drobnjak, I., Flitney, D. E., Niazy, R. K., Saunders, J., Vickers, J., Zhang, Y., De Stefano, N., Brady, J. M., & Matthews, P. M. (2004). Advances in functional and structural MR image analysis and implementation as FSL. *NeuroImage*, *23*(Suppl. 1), 208–219. https://doi.org/10.1016/j.neuroimage.2004.07.051, PubMed: 15501092

Sorrentino, P., Petkoski, S., Sparaco, M., Troisi Lopez, E., Signoriello, E., Baselice, F., Bonavita, S., Pirozzi, M. A., Quarantelli, M., Sorrentino, G., & Jirsa, V. (2022). Whole-brain propagation delays in multiple sclerosis, a combined tractography-magnetoencephalography study. *Journal of Neuroscience*, *42*(47), 8807–8816. https://doi.org/10.1523/JNEUROSCI.0938-22.2022, PubMed: 36241383

Sotiropoulos, S. N., & Zalesky, A. (2019). Building connectomes using diffusion MRI: Why, how and but. *NMR in Biomedicine*, *32*(4), e3752. https://doi.org/10.1002/nbm.3752, PubMed: 28654718

Sporns, O. (2010). *Networks of the brain*. MIT Press. https://doi.org/10.7551/mitpress/8476.001.0001

Sporns, O. (2011). The human connectome: A complex network. *Annals of the New York Academy of Sciences*, *1224*(1), 109–125.

https://doi.org/10.1111/j.1749-6632.2010.05888.x, PubMed: 21251014

Sporns, O. (2018). Graph theory methods: Applications in brain networks. *Dialogues in Clinical Neuroscience*, *20*(2), 111–120. https://doi.org/10.31887/DCNS.2018.20.2/osporns, PubMed: 30250388

Stikov, N., Campbell, J. S. W., Stroh, T., Lavelée, M., Frey, S., Novek, J., Nuara, S., Ho, M.-K., Bedell, B. J., Dougherty, R. F., Leppert, I. R., Boudreau, M., Narayanan, S., Duval, T., Cohen-Adad, J., Picard, P.-A., Gasecka, A., Côté, D., & Pike, G. B. (2015). In vivo histology of the myelin g-ratio with magnetic resonance imaging. *NeuroImage*, *118*, 397–405. https://doi.org/10.1016/j.neuroimage.2015.05.023, PubMed: 26004502

Stikov, N., Perry, L. M., Mezer, A., Rykhlevskaia, E., Wandell, B. A., Pauly, J. M., & Dougherty, R. F. (2011). Bound pool fractions complement diffusion measures to describe white matter micro and macrostructure. *NeuroImage*, *54*(2), 1112–1121. https://doi.org/10.1016/j.neuroimage.2010.08.068, PubMed: 20828622

Suárez, L. E., Markello, R. D., Betzel, R. F., & Misic, B. (2020). Linking structure and function in macroscale brain networks. *Trends in Cognitive Sciences*, *24*(4), 302–315. https://doi.org/10.1016/j.tics.2020.01.008, PubMed: 32160567

Tournier, J.-D., Calamante, F., & Connelly, A. (2010). Improved probabilistic streamlines tractography by 2nd order integration over fibre orientation distributions. *ISMRM*, *88*(2003), 2010. https://cds.ismrm.org/protected/10MProceedings/PDFfiles/1670_4298.pdf

Tournier, J. D., Calamante, F., & Connelly, A. (2012). MRtrix: Diffusion tractography in crossing fiber regions. *International Journal of Imaging Systems and Technology*, *22*(1), 53–66. https://doi.org/10.1002/ima.22005

Tournier, J. D., Mori, S., & Leemans, A. (2011). Diffusion tensor imaging and beyond. *Magnetic Resonance in Medicine*, *65*(6), 1532–1556. https://doi.org/10.1002/mrm.22924, PubMed: 21469191

Tournier, J. D., Smith, R., Raffelt, D., Tabbara, R., Dhollander, T., Pietsch, M., Christiaens, D., Jeurissen, B., Yeh, C.-H., & Connelly, A. (2019). *MRtrix3*: A fast, flexible and open software framework for medical image processing and visualisation. *NeuroImage*, *202*, 116137. https://doi.org/10.1016/j.neuroimage.2019.116137, PubMed: 31473352

Tustison, N. J., Avants, B. B., Cook, P. A., Zheng, Y., Egan, A., Yushkevich, P. A., & Gee, J. C. (2010). N4ITK: Improved N3 bias correction. *IEEE Transactions on Medical Imaging*, *29*(6), 1310–1320. https://doi.org/10.1109/TMI.2010.2046908, PubMed: 20378467

van den Heuvel, M. P., Kahn, R. S., Goñi, J., & Sporns, O. (2012). High-cost, high-capacity backbone for global brain communication. *Proceedings of the National Academy of Sciences*, *109*(28), 11372–11377. https://doi.org/10.1073/pnas.1203593109, PubMed: 22711833

van den Heuvel, M. P., Mandl, R. C. W., Stam, C. J., Kahn, R. S., & Hulshoff Pol, H. E. (2010). Aberrant frontal and temporal complex network structure in schizophrenia: A graph theoretical analysis. *Journal of Neuroscience*, *30*(47), 15915–15926. https://doi.org/10.1523/JNEUROSCI.2874-10.2010, PubMed: 21106830

van den Heuvel, M. P., & Sporns, O. (2011). Rich-club organization of the human connectome. *Journal of Neuroscience*, *31*(44), 15775–15786. https://doi.org/10.1523/JNEUROSCI.3539-11.2011, PubMed: 22049421

van den Heuvel, M. P., & Sporns, O. (2013). An anatomical substrate for integration among functional networks in human cortex. *Journal of Neuroscience*, *33*(36), 14489–14500. https://doi.org/10.1523/JNEUROSCI.2128-13.2013, PubMed: 24005300

van den Heuvel, M. P., Stam, C. J., Kahn, R. S., & Hulshoff Pol, H. E. (2009). Efficiency of functional brain networks and intellectual performance. *Journal of Neuroscience*, *29*(23), 7619–7624. https://doi.org/10.1523/JNEUROSCI.1443-09.2009, PubMed: 19515930

Veraart, J., Fieremans, E., & Novikov, D. S. (2016). Diffusion MRI noise mapping using random matrix theory. *Magnetic Resonance in Medicine*, *76*(5), 1582–1593. https://doi.org/10.1002/mrm.26059, PubMed: 26599599

Veraart, J., Novikov, D. S., Christiaens, D., Ades-Aron, B., Sijbers, J., & Fieremans, E. (2016). Denoising of diffusion MRI using random matrix theory. *NeuroImage*, *142*, 394–406. https://doi.org/10.1016/j.neuroimage.2016.08.016, PubMed: 27523449

Vos de Wael, R., Benkarim, O., Paquola, C., Lariviere, S., Royer, J., Tavakol, S., Xu, T., Hong, S.-J., Langs, G., Valk, S., Misic, B., Milham, M., Margulies, D. S., Smallwood, J., & Bernhardt, B. C. (2020). BrainSpace: A toolbox for the analysis of macroscale gradients in neuroimaging and connectomics datasets. *Communications Biology*, *3*(1), 103. https://doi.org/10.1038/s42003-020-0794-7, PubMed: 32139786

Wang, P., Kong, R., Kong, X., Liégeois, R., Orban, C., Deco, G., van den Heuvel, M. P., & Yeo, B. T. T. (2019). Inversion of a large-scale circuit model reveals a cortical hierarchy in the dynamic resting human brain. *Science Advances*, *5*(1), eaat7854. https://doi.org/10.1126/sciadv.aat7854, PubMed: 30662942

Xia, M., Wang, J., & He, Y. (2013). BrainNet Viewer: A network visualization tool for human brain connectomics. *PLOS ONE*, *8*(7), e68910. https://doi.org/10.1371/journal.pone.0068910, PubMed: 23861951

Yeh, C. H., Smith, R. E., Liang, X., Calamante, F., & Connelly, A. (2016). Correction for diffusion MRI fibre tracking biases: The consequences for structural connectomic metrics. *NeuroImage*, *142*, 150–162. https://doi.org/10.1016/j.neuroimage.2016.05.047, PubMed: 27211472

Yeh, F. C., Badre, D., & Verstynen, T. (2016). Connectometry: A statistical approach harnessing the analytical potential of the local connectome. *NeuroImage*, *125*, 162–171. https://doi.org/10.1016/j.neuroimage.2015.10.053, PubMed: 26499808

Yeo, B. T. T., Krienen, F. M., Sepulcre, J., Sabuncu, M. R., Lashkari, D., Hollinshead, M., Roffman, J. L., Smoller, J. W., Zöllei, L., Polimeni, J. R., Fisch, B., Liu, H., & Buckner, R. L. (2011). The organization of the human cerebral cortex estimated by intrinsic functional connectivity. *Journal of Neurophysiology*, *106*(3), 1125–1165. https://doi.org/10.1152/jn.00338.2011, PubMed: 21653723

Zalesky, A., Fornito, A., Cocchi, L., Gollo, L. L., van den Heuvel, M. P., & Breakspear, M. (2016). Connectome sensitivity or specificity: Which is more important? *NeuroImage*, *142*, 407–420. https://doi.org/10.1016/j.neuroimage.2016.06.035, PubMed: 27364472

Zhang, H., Schneider, T., Wheeler-Kingshott, C. A., & Alexander, D. C. (2012). NODDI: Practical *in vivo* neurite orientation dispersion and density imaging of the human brain. *NeuroImage, 61*(4), 1000–1016. https://doi.org/10.1016/j.neuroimage.2012.03.072, PubMed: 22484410

Zhang, Y., Brady, M., & Smith, S. (2001). Segmentation of brain MR images through a hidden Markov random field model and the expectation-maximization algorithm. *IEEE Transactions on Medical Imaging, 20*(1), 45–57. https://doi.org/10.1109/42.906424, PubMed: 11293691